

# Total and diffractive cross sections in enhanced Pomeron scheme

S. Ostapchenko\*

*NTNU, Institut for fysikk, 7021 Trondheim, Norway*

*D. V. Skobeltsyn Institute of Nuclear Physics, Moscow State University, 119992 Moscow, Russia*

September 15, 2018

## Abstract

For the first time, a systematic analysis of the high energy behavior of total and diffractive proton-proton cross sections is performed within the Reggeon Field Theory framework, based on the resummation of all significant contributions of enhanced Pomeron diagrams to all orders with respect to the triple-Pomeron coupling. The importance of different classes of enhanced graphs is investigated and it is demonstrated that absorptive corrections due to “net”-like enhanced diagrams and due to Pomeron “loops” are both significant and none of those classes can be neglected at high energies. A comparison with other approaches based on partial resummations of enhanced diagrams is performed. In particular, important differences are found concerning the predicted high energy behavior of total and single high mass diffraction proton-proton cross sections, with our values of  $\sigma_{pp}^{\text{tot}}$  at  $\sqrt{s} = 14$  TeV being some 25 ÷ 40% higher and with the energy rise of  $\sigma_{\text{HM}}^{\text{SD}}$  saturating well below the LHC energy. The main causes for those differences are analyzed and explained.

## 1 Introduction

Since long time theoretical investigations of high energy hadronic interactions remain at the frontier of particle physics research. This is especially true in the present situation, when the Large Hadron Collider (LHC) is becoming operative and new experimental installations are constructed for the studies of ultra-high energy cosmic rays. The ultimate goal of the corresponding theoretical research is to provide a fully microscopic description of the dynamics of hadronic collisions in the framework of the perturbative quantum chromodynamics (pQCD). However, at the present stage many important aspects of hadronic interactions can be addressed with effective approaches only. In particular, calculating total hadron-hadron cross section or treating diffractive particle production, one necessarily has to deal with important contributions from nonperturbative soft processes, which can not be described within the pQCD framework. The traditional phenomenological approach to such problems is provided by Gribov’s Reggeon Field Theory (RFT) [1]. In the RFT framework, hadron-hadron scattering in the high energy limit is dominated by multiple Pomeron exchanges, each Pomeron corresponding to an underlying microscopic parton cascade developing between the projectile and target hadrons. Within certain approximations, the scheme allows one to calculate various hadronic cross sections and to determine partial weights of hadronic final states of interest. This provided the ground for successful theoretical models for hadron-hadron scattering [2] and for corresponding Monte Carlo (MC) generators of high energy interactions [3]. However, proceeding to sufficiently high energies, one has to account for nonlinear contributions

---

\*e-mail: sergey.ostapchenko@ntnu.no

to the underlying parton dynamics, described by enhanced Pomeron diagrams [4, 5]. The difficulty which arises here is that enhanced graphs of more and more complicated topologies become increasingly important with rising energy. Thus, all-order resummation of enhanced contributions is a necessary condition for a self-consistent model.

A procedure for an asymptotic resummation of enhanced Pomeron diagrams has been proposed in [6]. More recently, extensive studies of total and diffractive proton-proton cross sections have been performed in [7, 8], including applications of the formalism for calculations of rapidity gap survival (RGS) probabilities. The corresponding treatment is based on a resummation of contributions of “net”-like enhanced graphs to elastic scattering amplitude, neglecting Pomeron “loop” diagrams. However, the employed parametrization for multi-Pomeron vertices implies a somewhat artificial hierarchy for the underlying parton cascades. On the other hand, the expressions for diffractive cross sections are derived in [7] from heuristic arguments, being in an explicit conflict with the traditional RFT treatment.

Similar studies of hadronic cross sections and of RGS probabilities have been performed also in [9], taking into account Pomeron loop contributions but neglecting net-like enhanced graphs. Thus, the approach is internally inconsistent: while cut diagrams of “fan” type (a subclass of general net-like graphs) are taken into consideration when calculating diffractive cross sections, those are neglected in the elastic scattering amplitude. In addition, the authors of Ref. [9] restricted themselves with the triple-Pomeron vertex only, neglecting other types of multi-Pomeron vertices. Such an approach is known to predict total hadron-hadron cross sections which become constant in the very high energy limit.

A general approach to the resummation of enhanced Pomeron diagrams has been proposed in [10, 11, 12], both for the corresponding contributions to elastic scattering amplitude and to partial cross sections of particular final states. In this paper, we apply the formalism for calculations of total and diffractive proton-proton cross sections at high energies. The principal differences of the present investigation compared to previous ones [7, 8, 9] are i) complete resummation of all important enhanced contributions to cross sections of interest, ii) self-consistent analysis of the structure of diffractive final states, based on the Abramovskii-Gribov-Kancheli (AGK) [13] cutting rules. The structure of the paper is as follows. In Section 2, we describe our model. In Section 3 and in the Appendix, we obtain expressions for high mass diffraction cross sections. In Section 4, we present our results for total and diffractive proton-proton cross sections and investigate relative importance of various classes of enhanced graphs. In Section 5, the differences with other approaches are analyzed. Finally, the conclusions are presented in Section 6.

## 2 The model

### 2.1 Multi-channel eikonal approach

In the RFT framework, hadron-hadron scattering is dominated in the high energy limit by multiple Pomeron exchanges between the projectile and target hadrons, as depicted in Fig. 1. Using

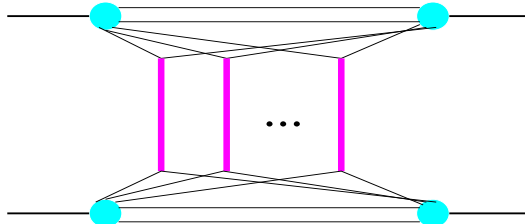


Figure 1: General multi-Pomeron contribution to hadron-hadron scattering amplitude; elementary scattering processes (vertical thick lines) are described as Pomeron exchanges.

eikonal Pomeron-hadron vertices and employing multi-channel scheme to account for contributions of inelastic intermediate hadronic states of small masses<sup>1</sup> between Pomeron emissions, elastic proton-proton scattering amplitude  $T(s, t)$  can be expressed as [14, 15]

$$T(s, t) = 2s \int d^2b e^{i\vec{q}\vec{b}} f(s, b) = 2is \int d^2b e^{i\vec{q}\vec{b}} \sum_{j,k} C_j C_k \left[ 1 - e^{-\chi_{jk}^{\mathbb{P}}(s, b)} \right]. \quad (1)$$

Here  $s, t = q^2$ , and  $b$  are correspondingly c.m. energy squared, momentum transfer, and impact parameter for the interaction,  $f(s, b)$  - elastic scattering amplitude in the impact parameter representation.  $C_j$  defines partial weight for proton elastic scattering eigenstate  $|j\rangle$  ( $|p\rangle = \sum_j \sqrt{C_j} |j\rangle$ ,  $\sum_j C_j = 1$ ) and  $\chi_{jk}^{\mathbb{P}}$  is the so-called eikonal corresponding to Pomeron exchange between the projectile and target protons, the latter being represented by eigenstates  $|j\rangle$  and  $|k\rangle$ . The eikonal  $\chi_{jk}^{\mathbb{P}}$  is expressed via the Pomeron propagator  $D^{\mathbb{P}}(s, t)$  and the vertex  $F_j^{\mathbb{P}}(t)$  for Pomeron emission by eigenstate  $|j\rangle$  as

$$\chi_{jk}^{\mathbb{P}}(s, b) = \frac{1}{8\pi^2 i s} \int d^2q e^{-i\vec{q}\vec{b}} F_j^{\mathbb{P}}(q^2) F_k^{\mathbb{P}}(q^2) D^{\mathbb{P}}(s, q^2). \quad (2)$$

In this work, we use 2-component model ( $j, k = 1, 2$ ) and employ the dipole parametrization for the  $t$ -dependence of  $F_j^{\mathbb{P}}$ :

$$F_j^{\mathbb{P}}(t) = \frac{\gamma_j}{(1 - \Lambda_j t)^2}. \quad (3)$$

Concerning  $D^{\mathbb{P}}(s, t)$ , we assume it to receive contributions from two Pomeron poles: a ‘‘soft’’ Pomeron, which corresponds to the underlying cascade of partons of small virtualities, and a ‘‘hard’’ one, which is dominated by relatively hard partons of higher  $\langle |q^2| \rangle$ . Neglecting small real parts of Pomeron pole amplitudes and introducing a parameter  $r_{h/s} \ll 1$  for the ratio of proton couplings to the hard and soft Pomerons, we have

$$D^{\mathbb{P}}(s, t) = 8\pi i \left[ s^{\alpha_{\mathbb{P}(s)}} e^{\alpha'_{\mathbb{P}(s)} \ln s t} + r_{h/s} s^{\alpha_{\mathbb{P}(h)}} e^{\alpha'_{\mathbb{P}(h)} \ln s t} \right], \quad (4)$$

with  $\alpha_{\mathbb{P}(s/h)}$  and  $\alpha'_{\mathbb{P}(s/h)}$  being intercepts and slopes of the Pomeron Regge trajectories. In the following we assume both Pomeron trajectories to be overcritical,  $\Delta_{s/h} = \alpha_{\mathbb{P}(s/h)} - 1 > 0$ , with the hard Pomeron characterized by a steeper energy dependence,  $\Delta_h > \Delta_s$ , and a smaller slope,  $\alpha'_{\mathbb{P}(h)} < \alpha'_{\mathbb{P}(s)}$ .

Knowing the elastic amplitude, one can easily calculate total and elastic cross sections and the elastic scattering slope:

$$\sigma^{\text{tot}}(s) = 2 \text{Im} \int d^2b f(s, b) = 2 \int d^2b \sum_{j,k} C_j C_k \left( 1 - e^{-\chi_{jk}^{\mathbb{P}}(s, b)} \right) \quad (5)$$

$$\sigma^{\text{el}}(s) = \int d^2b |f(s, b)|^2 = \int d^2b \left[ \sum_{j,k} C_j C_k \left( 1 - e^{-\chi_{jk}^{\mathbb{P}}(s, b)} \right) \right]^2 \quad (6)$$

$$B^{\text{el}}(s) = \left. \frac{d \ln(d\sigma^{\text{el}}(s, t)/dt)}{dt} \right|_{t=0} = \frac{2}{\sigma^{\text{tot}}(s)} \int d^2b b^2 \sum_{j,k} C_j C_k \left( 1 - e^{-\chi_{jk}^{\mathbb{P}}(s, b)} \right). \quad (7)$$

Moreover, making use of the optical theorem and of the AGK cutting rules [13], one can relate contributions of certain unitarity cuts of elastic scattering diagrams of Fig. 1 to partial cross sections of particular hadronic final states. For example, cross sections for single and double low

<sup>1</sup>Here we restrict ourselves with low mass inelastic states in order to use an energy-independent decomposition of proton wave function in terms of the corresponding elastic scattering eigenstates.

mass diffractive dissociation are obtained considering cut diagrams in which the cut plane passes between  $m \geq 2$  uncut Pomerons and choosing in the cut plane inelastic intermediate states for one or for both protons correspondingly [14]:

$$\sigma_{\text{LM}}^{\text{SD}}(s) = 2 \int d^2b \sum_{j,k,l,m} (C_j \delta_{jl} - C_j C_l) C_k C_m \left(1 - e^{-\chi_{jk}^{\mathbb{P}}(s,b)}\right) \left(1 - e^{-\chi_{lm}^{\mathbb{P}}(s,b)}\right) \quad (8)$$

$$\sigma_{\text{LM}}^{\text{DD}}(s) = \int d^2b \sum_{j,k,l,m} (C_j \delta_{jl} - C_j C_l) (C_k \delta_{km} - C_k C_m) \left(1 - e^{-\chi_{jk}^{\mathbb{P}}(s,b)}\right) \left(1 - e^{-\chi_{lm}^{\mathbb{P}}(s,b)}\right). \quad (9)$$

## 2.2 Enhanced diagram contributions to elastic scattering amplitude

The above-discussed picture corresponds to multiple parton cascades developing independently between the projectile and target hadrons. However, proceeding to sufficiently high energies, one inevitably faces the situation when such cascades overlap and influence each other. Such nonlinear effects are traditionally described by enhanced Pomeron diagrams which account for Pomeron-Pomeron interactions [4, 5, 6]. Taking such contributions into account, hadronic cross sections are still given by Eqs. (5-9), however, with the simple Pomeron exchange eikonal  $\chi_{jk}^{\mathbb{P}}(s, b)$  being replaced by half the total opacity

$$\frac{1}{2} \Omega_{jk}(s, b) = \chi_{jk}^{\mathbb{P}}(s, b) + \chi_{jk}^{\text{enh}}(s, b), \quad (10)$$

where the eikonal  $\chi_{jk}^{\text{enh}}(s, b)$  represents the contribution of all irreducible enhanced Pomeron graphs exchanged between the eigenstates  $|j\rangle$  and  $|k\rangle$  of the projectile and target protons.

A general procedure for a resummation of enhanced Pomeron diagrams, both for elastic scattering amplitude and for corresponding unitarity cuts, has been proposed in [10, 12]. In this work, we consider eikonal multi-Pomeron vertices, assuming the vertex slope to be small and neglecting it in the following. Thus, the transition of  $m$  into  $n$  Pomerons ( $m+n \geq 3$ ) is described by a vertex [6]

$$G^{(m,n)} = G \gamma_{\mathbb{P}}^{m+n}, \quad (11)$$

the constant  $G$  being related to the triple-Pomeron coupling  $r_{3\mathbb{P}}$  as  $G = r_{3\mathbb{P}}/(4\pi\gamma_{\mathbb{P}}^3)$ .<sup>2</sup> Hence, for a Pomeron exchanged between the projectile or the target proton (represented by diffractive eigenstate  $|j\rangle$ ) and a multi-Pomeron vertex separated from it by rapidity and impact parameter distances  $y$  and  $b$  we obtain the eikonal

$$\chi_j^{\mathbb{P}}(y, b) = \frac{\gamma_{\mathbb{P}}}{8\pi^2 i e^y} \int d^2q e^{-iq\vec{b}} F_j^{\mathbb{P}}(q^2) D^{\mathbb{P}}(e^y, q^2), \quad (12)$$

where we included the vertex factor  $\gamma_{\mathbb{P}}$  in the definition of the eikonal. Similarly, for a Pomeron exchanged between two vertices separated by rapidity and impact parameter distances  $y$  and  $b$  we have

$$\chi^{\mathbb{P}}(y, b) = \frac{\gamma_{\mathbb{P}}^2}{8\pi^2 i e^y} \int d^2q e^{-iq\vec{b}} D^{\mathbb{P}}(e^y, q^2). \quad (13)$$

As demonstrated in [10], a general irreducible contribution of arbitrary net-like enhanced diagrams (i.e. all possible enhanced graphs with the exception of Pomeron loop contributions) can be written down in a rather compact form, being expressed via contributions of sub-graphs of certain structure, so-called “net-fans”. The latter are defined by a Schwinger-Dyson equation which resembles to some extent the usual fan diagram equation (therefore, the name – “net-fans”) and correspond to arbitrary irreducible nets of Pomerons, exchanged between the projectile and target hadrons, with one vertex in the net having a fixed position in the rapidity and impact parameter

<sup>2</sup>In the limit  $\gamma_{\mathbb{P}} \rightarrow 0$ ,  $r_{3\mathbb{P}}$  being fixed, one arrives to the scheme with the triple-Pomeron vertex only.

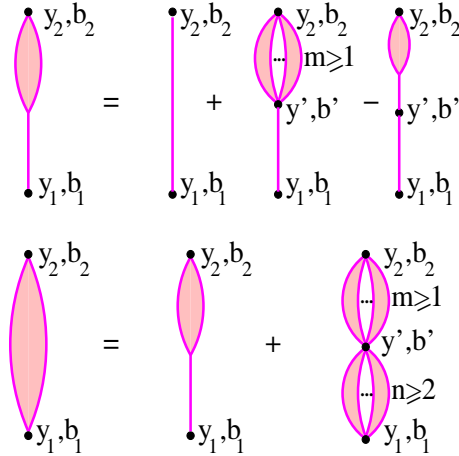


Figure 2: Recursive representations for the contributions of Pomeron loop sequences  $\chi^{\text{loop}(1)}$  (top) and  $\chi^{\text{loop}}$  (bottom), exchanged between the vertices  $(y_1, \vec{b}_1)$  and  $(y_2, \vec{b}_2)$ .

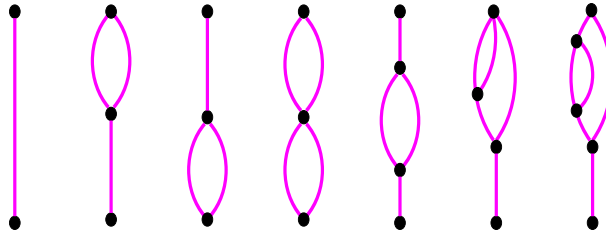


Figure 3: Examples of graphs generated by Schwinger-Dyson equations of Fig. 2.

space. Furthermore, it has been shown in [12] that the scheme can be generalized to include rather general Pomeron loop contributions by merely replacing single Pomerons connecting neighboring net “cells” by arbitrary 2-point sequences of Pomerons and Pomeron loops.

Let us introduce the contribution  $\chi^{\text{loop}}(y_2 - y_1, |\vec{b}_2 - \vec{b}_1|)$  of *irreducible* 2-point sequences of Pomerons and Pomeron loops, exchanged between two vertices which are separated by rapidity and impact parameter distances  $y_2 - y_1$  and  $|\vec{b}_2 - \vec{b}_1|$ , with the help of recursive equations of Fig. 2<sup>3</sup>. The equation in the 1st line in Fig. 2 defines the contribution  $\chi^{\text{loop}(1)}(y_2 - y_1, |\vec{b}_2 - \vec{b}_1|)$  of such sub-sequences which start from a single Pomeron connected to the vertex  $(y_1, \vec{b}_1)$ . The first term in the r.h.s. of the equation is just a single Pomeron exchange between the two vertices, whereas the second consists of a single Pomeron exchanged between the vertex  $(y_1, \vec{b}_1)$  and an intermediate multi-Pomeron vertex  $(y', \vec{b}')$  plus  $m \geq 1$  irreducible loop sequences (each one described by the eikonal  $\chi^{\text{loop}}(y_2 - y', |\vec{b}_2 - \vec{b}'|)$ ) exchanged between the vertices  $(y', \vec{b}')$  and  $(y_2, \vec{b}_2)$ . The last term in the r.h.s. is to subtract the Pomeron self-coupling contribution. In turn, the equation in the 2nd line in Fig. 2 defines the complete contribution  $\chi^{\text{loop}}(y_2 - y_1, |\vec{b}_2 - \vec{b}_1|)$ , adding to the above-discussed terms also the 2nd graph in the r.h.s. of the equation, which contains  $n \geq 2$  irreducible loop sequences exchanged between the vertices  $(y_1, \vec{b}_1)$  and  $(y', \vec{b}')$  plus  $m \geq 1$  sequences exchanged between the vertices  $(y', \vec{b}')$  and  $(y_2, \vec{b}_2)$ . Examples of graphs generated by the described equations are depicted in Fig. 3. Following the general rules of the Reggeon diagram technique [1, 16], we

<sup>3</sup>The present definition is somewhat more general compared to the one in Ref. [12].

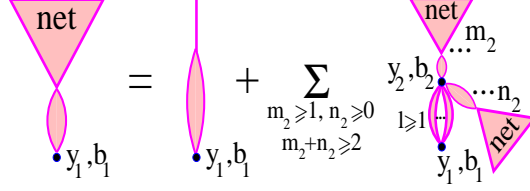


Figure 4: Recursive equation for projectile net-fan contribution  $\chi_{jk}^{\text{net}}(y_1, \vec{b}_1|Y, \vec{b})$ ;  $y_1$  and  $b_1$  are rapidity and impact parameter distances between the projectile proton and the vertex in the “handle” of the fan. The vertex  $(y_2, \vec{b}_2)$  couples together  $m_2$  projectile net-fans and  $n_2$  target net-fans. In addition, there are  $l \geq 1$  irreducible 2-point sequences of Pomerons and Pomeron loops, exchanged between the vertices  $(y_1, \vec{b}_1)$  and  $(y_2, \vec{b}_2)$ .

obtain

$$\chi^{\text{loop}(1)}(y_2 - y_1, |\vec{b}_2 - \vec{b}_1|) = \chi^{\mathbb{P}}(y_2 - y_1, |\vec{b}_2 - \vec{b}_1|) + G \int_{y_1 + \xi}^{y_2 - \xi} dy' \int d^2 b' \chi^{\mathbb{P}}(y' - y_1, |\vec{b}' - \vec{b}_1|) \times \left[ 1 - e^{-\chi^{\text{loop}}(y_2 - y', |\vec{b}_2 - \vec{b}'|)} - \chi^{\text{loop}(1)}(y_2 - y', |\vec{b}_2 - \vec{b}'|) \right] \quad (14)$$

$$\chi^{\text{loop}}(y_2 - y_1, |\vec{b}_2 - \vec{b}_1|) = \chi^{\text{loop}(1)}(y_2 - y_1, |\vec{b}_2 - \vec{b}_1|) + G \int_{y_1 + \xi}^{y_2 - \xi} dy' \int d^2 b' \times \left[ 1 - e^{-\chi^{\text{loop}}(y' - y_1, |\vec{b}' - \vec{b}_1|)} - \chi^{\text{loop}}(y' - y_1, |\vec{b}' - \vec{b}_1|) \right] \left[ 1 - e^{-\chi^{\text{loop}}(y_2 - y', |\vec{b}_2 - \vec{b}'|)} \right]. \quad (15)$$

It is noteworthy that the  $y'$ -integration in the r.h.s. of (14-15) is performed between  $y_1 + \xi$  and  $y_2 - \xi$ , with  $\xi$  being the minimal rapidity interval for the Pomeron asymptotics to be applicable.

Now, we can define the net-fan contribution via the recursive representation of Fig. 4 [12]:

$$\chi_{jk}^{\text{net}}(y_1, \vec{b}_1|Y, \vec{b}) = \chi_j^{\text{loop}}(y_1, b_1) + G \int_{\xi}^{y_1 - \xi} dy_2 \int d^2 b_2 \left( 1 - e^{-\chi^{\text{loop}}(y_1 - y_2, |\vec{b}_1 - \vec{b}_2|)} \right) \times \left[ \left( 1 - e^{-\chi_{jk}^{\text{net}}(y_2, \vec{b}_2|Y, \vec{b})} \right) e^{-\chi_{kj}^{\text{net}}(Y - y_2, \vec{b} - \vec{b}_2|Y, \vec{b})} - \chi_{jk}^{\text{net}}(y_2, \vec{b}_2|Y, \vec{b}) \right]. \quad (16)$$

By definition,  $\chi_{jk}^{\text{net}}(y_1, \vec{b}_1|Y, \vec{b})$  represents the total contribution of irreducible net-like graphs exchanged between the projectile and the target (represented by eigenstates  $|j\rangle$  and  $|k\rangle$ ), with  $Y = \ln s$  and  $\vec{b}$  being the impact parameter for the collision. The projectile (target) net-fan starts from a given vertex and develops initially towards the projectile (target) which is separated from the vertex by rapidity and impact parameter distances  $y_1$  and  $b_1$ . The 1st term in the r.h.s. of the equation in Fig. 4 corresponds to a single 2-point sequence of Pomerons and Pomeron loops exchanged between the projectile (target) proton and the vertex  $(y_1, \vec{b}_1)$ , such that only one Pomeron is coupled to the proton. The 2nd term describes the development of the Pomeron net: for  $m_2 \geq 2$  one has a fan-like splitting and  $m_2$  projectile (target) net-fans originate from the vertex  $(y_2, \vec{b}_2)$ , developing initially in the direction of the projectile (target); for  $n_2 \geq 1$  one obtains in addition a re-scattering on the partner proton -  $n_2$  target (projectile) net-fans start from the vertex and develop initially in the target (projectile) direction. The 2-point loop sequence exchanged between the original vertex  $(y_1, \vec{b}_1)$  and the nearest net cell (the vertex  $(y_2, \vec{b}_2)$  in Fig. 4) will be referred to as the “handle” of the fan.

The contribution  $\chi_j^{\text{loop}}(y_1, b_1)$  of the first graph in the r.h.s. of the equation in Fig. 4 and a part of it,  $\chi_j^{\text{loop}(1)}(y_1, b_1)$ , corresponding to 2-point Pomeron loop sequences which start from a single Pomeron connected to the vertex  $(y_1, \vec{b}_1)$ , are defined in Fig. 5 (cf. Fig. 2), which gives

$$\chi_j^{\text{loop}}(y_1, b_1) = \chi_j^{\mathbb{P}}(y_1, b_1) + G \int_{\xi}^{y_1 - \xi} dy' \int d^2 b' \chi_j^{\mathbb{P}}(y', b')$$

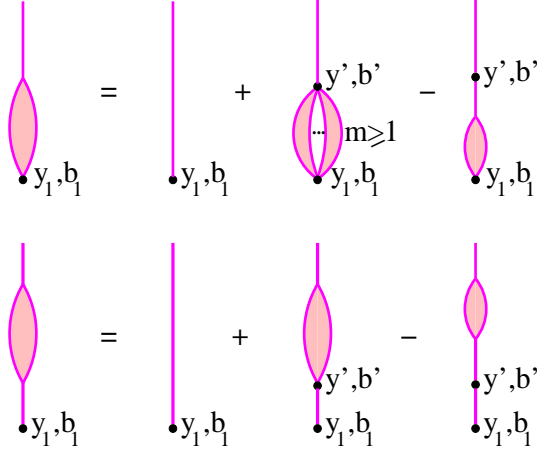


Figure 5: Contributions of 2-point sequences of Pomerons and Pomeron loops  $\chi_j^{\text{loop}}$  (top) and  $\chi_j^{\text{loop}(1)}$  (bottom), exchanged between the projectile and the vertex  $(y_1, \vec{b}_1)$ .

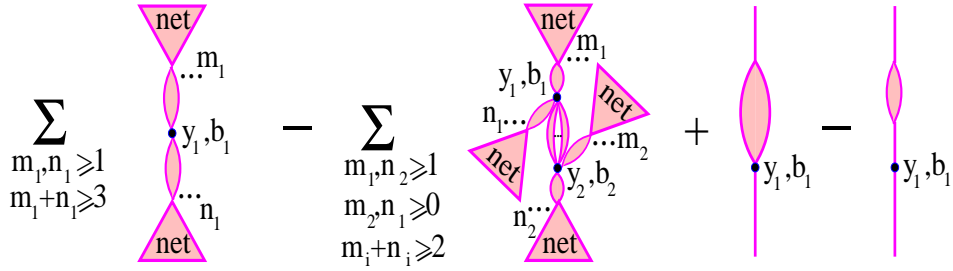


Figure 6: Total contribution of irreducible enhanced diagrams to elastic scattering amplitude.

$$\times \left[ 1 - e^{-\chi^{\text{loop}}(y_1 - y', |\vec{b}_1 - \vec{b}'|)} - \chi^{\text{loop}(1)}(y_1 - y', |\vec{b}_1 - \vec{b}'|) \right] \quad (17)$$

$$\chi_j^{\text{loop}(1)}(y_1, b_1) = \chi_j^{\mathbb{P}}(y_1, b_1) + G \int_{\xi}^{y_1 - \xi} dy' \int d^2 b' \left[ \chi_j^{\text{loop}}(y', b') - \chi_j^{\text{loop}(1)}(y', b') \right] \times \chi^{\mathbb{P}}(y_1 - y', |\vec{b}_1 - \vec{b}'|). \quad (18)$$

Finally, for the total contribution of irreducible enhanced graphs  $\chi_{jk}^{\text{enh}}$  (exchanged between eigenstates  $|j\rangle$  and  $|k\rangle$  of the projectile and of the target respectively) to elastic scattering amplitude one obtains the diagrammatic representation of Fig. 6 [12], which gives

$$\begin{aligned} \chi_{jk}^{\text{enh}}(s, b) = & G \int_{\xi}^{Y - \xi} dy_1 \int d^2 b_1 \left\{ \left[ \left( 1 - e^{-\chi_{jk}^{\text{net}}(1)} \right) \left( 1 - e^{-\chi_{kj}^{\text{net}}(1)} \right) - \chi_{jk}^{\text{net}}(1) \chi_{kj}^{\text{net}}(1) \right] \right. \\ & - G \int_{\xi}^{y_1 - \xi} dy_2 \int d^2 b_2 \left( 1 - e^{-\chi^{\text{loop}}(y_1 - y_2, |\vec{b}_1 - \vec{b}_2|)} \right) \left[ \left( 1 - e^{-\chi_{jk}^{\text{net}}(1)} \right) e^{-\chi_{kj}^{\text{net}}(1)} - \chi_{jk}^{\text{net}}(1) \right] \\ & \times \left[ \left( 1 - e^{-\chi_{kj}^{\text{net}}(2)} \right) e^{-\chi_{jk}^{\text{net}}(2)} - \chi_{kj}^{\text{net}}(2) \right] \\ & \left. + \chi_k^{\mathbb{P}}(y_1, b_1) \left[ \chi_j^{\text{loop}}(Y - y_1, |\vec{b} - \vec{b}_1|) - \chi_j^{\text{loop}(1)}(Y - y_1, |\vec{b} - \vec{b}_1|) \right] \right\}, \quad (19) \end{aligned}$$

where we used the abbreviations  $\chi_{jk}^{\text{net}}(i) = \chi_{jk}^{\text{net}}(Y - y_i, \vec{b} - \vec{b}_i | Y, \vec{b})$ ,  $\chi_{kj}^{\text{net}}(i) = \chi_{kj}^{\text{net}}(y_i, \vec{b}_i | Y, \vec{b})$ ,  $i = 1, 2$ .

The first diagram in Fig. 6 generates all possible Pomeron nets exchanged between the projectile and target protons (with neighboring net cells connected by 2-point sequences of Pomerons and

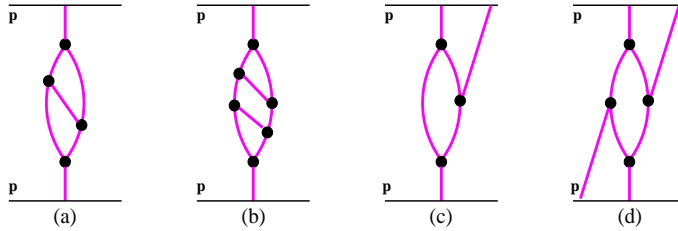


Figure 7: Examples of diagrams which are not included in the described resummation scheme.

Pomeron loops), coupling together  $m_1$  projectile and  $n_1$  target net-fans ( $m_1 + n_1 \geq 3$ ) in the vertex  $(y_1, \vec{b}_1)$ , whereas the second graph subtracts contributions which are generated two or more times. The third diagram corresponds to a single 2-point sequence of Pomerons and Pomeron loops exchanged between the projectile and the target, each of the two being coupled to a single Pomeron only. The last graph subtracts the Pomeron self-coupling contribution generated by the previous diagram.

The described scheme takes into consideration all possible enhanced diagrams with the exception of two classes illustrated in Fig. 7. The graphs in Fig. 7 (a,b) contain Pomeron loops whose “sides” are “glued” together by additional Pomeron exchanges; such diagrams are not generated by the simple Schwinger-Dyson equations of Fig. 2. The graphs in Fig. 7 (c,d) contain loops whose “surface” is coupled to the projectile and/or target by additional Pomeron exchanges. Such contributions can not be easily resummed to all orders in the described scheme and require a serious modification of the resummation procedure. However, both classes of diagrams will be shown to provide negligible contributions to elastic scattering amplitude in the described approach.

### 3 High mass diffraction

#### 3.1 High mass diffraction cross sections

The beauty of the RFT approach is that it allows one to calculate not only enhanced diagram contributions to elastic scattering amplitude but also partial cross sections for various final states, particularly, ones which contain large rapidity gaps (LRG) not covered by secondary particle production. One derives the latter by considering unitarity cuts of elastic scattering graphs and collecting contributions of cuts corresponding to the desirable structure of final states. For example, cross sections for single, double, and central diffraction (often referred to as the double Pomeron exchange (DPE)) are defined by cut diagrams of the kinds depicted in Fig. 8 (a), (b), and (c) correspondingly. In Fig. 8 (a) particle production emerges from the cut Pomeron block  $C$ , covering

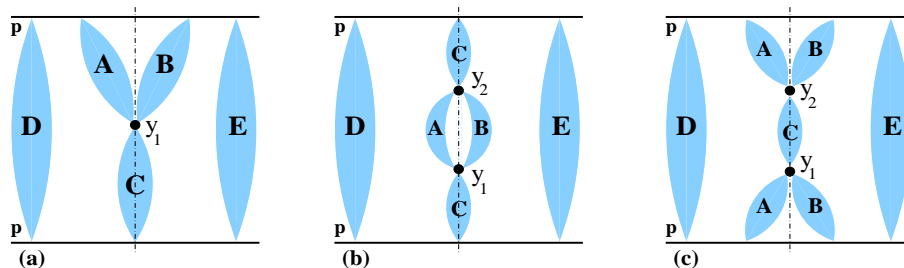


Figure 8: Classes of cut diagrams corresponding to single target diffraction (a), double diffraction (b), and central diffraction (c) cross sections. Thin dot-dashed lines indicate the position of the cut plane.



the rapidity range  $(0, y_1)$ . On the other hand, in the rapidity interval  $(y_1, Y)$  no particle is produced: the cut plane passes between the uncut Pomeron blocks  $A$  and  $B$ . In parallel to the cut irreducible graph  $ABC$ , one may have a number of uncut irreducible graphs exchanged to the left ( $D$ ) and to the right ( $E$ ) of the cut plane, which represent elastic rescattering processes. The corresponding factor may be interpreted as the probability not to have other multiple production processes in addition to the diffractive  $ABC$  topology. Similarly, in Fig. 8 (b) particles are produced in the rapidity intervals  $(0, y_1)$  and  $(y_2, Y)$ , whereas in the rapidity range  $(y_1, y_2)$  the cut plane passes between uncut Pomeron blocks, forming a LRG. Finally, in Fig. 8 (c) particle production takes place in the central rapidity interval  $(y_1, y_2)$ , which is separated from the quasi-elastically scattered projectile and target protons by large rapidity gaps  $(0, y_1)$  and  $(y_2, Y)$ .

The representation of Fig. 8 is schematic for three reasons. First, all the Pomeron blocks in the diffractively cut sub-graphs may be connected both to the projectile and to the target protons by additional *uncut* Pomeron exchanges. For example, the blocks  $A$  and  $B$  in Fig. 8 (a) may have internal multi-Pomeron vertices, with one or a number of uncut Pomerons coupled to those vertices and to the target proton. Secondly, contributions to diffractive cross sections come also from multiple exchanges of diffractively cut sub-graphs, e.g. from multiple exchanges of the  $ABC$ -like Pomeron configurations, each one with a rapidity gap of desirable size or larger, in case of single diffraction. Third, one generally has to choose proper intermediate states in the cut plane for the projectile or/and target protons. For example, in Fig. 8 (a) one has to choose elastic intermediate state for the projectile proton in order to obtain single diffraction cross section. On the contrary, choosing an inelastic intermediate state, one gets a contribution to double diffraction cross section, with a high mass diffractive state produced in the backward hemisphere and a small mass one in the projectile fragmentation region.

Keeping those remarks in mind, we can express various diffractive cross sections via contributions of irreducible cut diagrams characterized by the desirable structure of rapidity gaps. Let us denote the contribution of all  $ABC$ -like cut graphs, with a forward rapidity gap of size  $y_{\text{gap}}$  or larger and without a LRG separating the target proton from other particles produced, as  $2\chi_{j_1 j_2 k}^{1-\text{gap}}(Y, b, y_{\text{gap}})$ , where  $b$  is the impact parameter for the collision,  $j_1$  and  $j_2$  are the projectile elastic scattering eigenstates to the left and to the right of the cut plane,<sup>4</sup> and  $k$  is the target elastic scattering eigenstate. Similarly, we shall use the notation  $2\chi_{j_1 j_2 k_1 k_2}^{2-\text{gap}}(Y, b, y_{\text{gap}}^{(f)}, y_{\text{gap}}^{(b)})$  for the contribution of  $ABCAB$ -like cut graphs of Fig. 8 (c) with the rapidity gaps in the forward and backward directions of the sizes  $y_{\text{gap}}^{(f)}$  and  $y_{\text{gap}}^{(b)}$  or larger. Finally, the contribution of  $CABC$ -like cut graphs of Fig. 8 (b), corresponding to high mass diffractive states both in the forward and in the backward direction and a central LRG of size  $y_{\text{gap}}$  or larger, is denoted as  $2\chi_{jk}^{c-\text{gap}}(Y, b, y_{\text{gap}})$ . Then, single high mass diffraction cross section is given as

$$\sigma_{\text{HM}}^{\text{SD}}(s, y_{\text{gap}}) = 2 \sum_{j_1, j_2, k} C_{j_1} C_{j_2} C_k \int d^2b \left[ e^{2\chi_{j_1 j_2 k}^{1-\text{gap}}(Y, b, y_{\text{gap}}) + 2\chi_{j_1 j_2 k k}^{2-\text{gap}}(Y, b, y_{\text{gap}}, \xi)} - 1 \right] S_{j_1 j_2 k k}(s, b) - 2\sigma^{\text{DPE}}(s, y_{\text{gap}}, \xi), \quad (20)$$

where for the so-called eikonal RGS factor corresponding to the contribution of the uncut Pomeron blocks (D) and (E) in Fig. 8 and describing the probability not to fill the gap by secondary particles produced in additional inelastic rescattering processes we have

$$S_{j_1 j_2 k_1 k_2}(s, b) \equiv e^{-\frac{1}{2}\Omega_{j_1 k_1}(s, b) - \frac{1}{2}\Omega_{j_2 k_2}(s, b)}, \quad (21)$$

with the total opacity being defined in (10). The factor in the square brackets in the r.h.s. of Eq. (20) comes from an exchange of an arbitrary number ( $\geq 1$ ) of cut graphs characterized by a rapidity gap in the forward direction of size  $y_{\text{gap}}$  or larger. In the cut plane we choose proton (elastic) state

<sup>4</sup>In general, we have to consider different elastic scattering eigenstates to the left and to the right of the cut plane, in order to project on the elastic proton or low mass diffraction intermediate state. Naturally, summing over all intermediate hadronic states, we obtain a diagonal transition matrix:  $\delta_{j_1 j_2} = C_{j_1} C_{j_2} + (C_{j_1} \delta_{j_1 j_2} - C_{j_1} C_{j_2})$ .

for the projectile (c.f. Eq. (8)). Finally, from the obtained expression we subtract the contribution of the central diffraction, with elastic proton states in the cut plane both for the projectile and for the target and with rapidity gaps of sizes  $y_{\text{gap}}$  and  $\xi$  correspondingly, which separate those protons from the produced particles. The factor '2' in the two terms in the r.h.s. accounts for both projectile and target single diffraction contributions.

In turn, the above-discussed central diffraction cross section is

$$\sigma^{\text{DPE}}(s, y_{\text{gap}}^{(f)}, y_{\text{gap}}^{(b)}) = \sum_{j_1, j_2, k_1, k_2} C_{j_1} C_{j_2} C_{k_1} C_{k_2} \int d^2b \left[ e^{2\chi_{j_1 j_2 k_1 k_2}^{2-\text{gap}}(Y, b, y_{\text{gap}}^{(f)}, y_{\text{gap}}^{(b)})} - 1 \right] S_{j_1 j_2 k_1 k_2}(s, b). \quad (22)$$

Finally, for the double high mass diffraction cross section, with central LRG of size  $y_{\text{gap}}$  or larger, we obtain

$$\begin{aligned} \sigma_{\text{HM}}^{\text{DD}}(s, y_{\text{gap}}) &= \sum_{j, k} C_j C_k \int d^2b \, 2\chi_{jk}^{c-\text{gap}}(Y, b, y_{\text{gap}}) S_{jjkk}(s, b) \\ &+ 2 \sum_{j_1, j_2, k} (C_{j_1} \delta_{j_1 j_2} - C_{j_1} C_{j_2}) C_k \int d^2b \left[ e^{2\chi_{j_1 j_2 k}^{1-\text{gap}}(Y, b, y_{\text{gap}})} - 1 \right] e^{2\chi_{j_1 j_2 k k}^{2-\text{gap}}(Y, b, y_{\text{gap}}, \xi)} S_{j_1 j_2 k k}(s, b) \\ &\quad + \sum_{j_1, j_2, k_1, k_2} (C_{j_1} \delta_{j_1 j_2} - C_{j_1} C_{j_2}) (C_{k_1} \delta_{k_1 k_2} - C_{k_1} C_{k_2}) \\ &\quad \times \int d^2b \left[ e^{2\chi_{j_1 j_2 k_1 k_2}^{2-\text{gap}}(Y, b, y_{\text{gap}}, \xi)} + e^{2\chi_{j_1 j_2 k_1 k_2}^{2-\text{gap}}(Y, b, \xi, y_{\text{gap}})} - e^{2\chi_{j_1 j_2 k_1 k_2}^{2-\text{gap}}(Y, b, y_{\text{gap}}, y_{\text{gap}})} - 1 \right] S_{j_1 j_2 k_1 k_2}(s, b) \\ &+ \sum_{j, k} C_j C_k \int d^2b \int_{\xi}^{Y-y_{\text{gap}}-\xi} dy_1 \int_{y_1+y_{\text{gap}}}^{Y-\xi} dy_2 \frac{2d\chi_{jjk}^{1-\text{gap}}(Y, b, Y-y_1)}{d(Y-y_1)} \frac{2d\chi_{kkj}^{1-\text{gap}}(Y, b, y_2)}{dy_2} S_{jjkk}(s, b), \quad (23) \end{aligned}$$

where in the 1st term in the r.h.s., corresponding to the production of high mass diffractive states both in the forward and in the backward hemisphere, we neglected multiple exchanges of cut sub-graphs with a central rapidity gap. The 2nd term describes the production of high mass diffractive state in the backward and a low mass one in the forward direction (c.f. (8)); it is multiplied by factor '2' to account for the opposite configuration. The 3rd term corresponds to the low mass diffractive dissociation of both the projectile and the target protons, which is accompanied by the production of a diffractive bunch of secondaries in the central region. The latter is separated from the projectile or/and target diffractive state by a LRG of size  $\geq y_{\text{gap}}$ . Finally, the last term in (23) describes the situation when projectile and target high mass diffractive states are produced in two different inelastic rescattering processes (we neglect here contributions with three or more diffractively cut sub-graphs), i.e. to a superposition of two (projectile and target) single diffraction processes.<sup>5</sup> There, we consider differential contributions  $2d\chi_{j_1 j_2 k}^{1-\text{gap}}(Y, b, y_{\text{gap}})/dy_{\text{gap}}$  for a fixed size of the gap; the limits for the rapidity integrations in the last term in (23) are chosen such that a rapidity gap of size  $\geq y_{\text{gap}}$  remains in the central region.

### 3.2 Simplest enhanced graphs with LRG topologies

We shall illustrate here the structure of the contributions  $\chi^{1-\text{gap}}$ ,  $\chi^{2-\text{gap}}$ , and  $\chi^{c-\text{gap}}$  by considering the simplest enhanced graphs of the corresponding kinds, up to the second order with respect to the triple-Pomeron coupling, while the complete all-order treatment will be discussed in the Appendix.

The simplest contribution to  $2\chi_{j_1 j_2 k}^{1-\text{gap}}(Y, b, y_{\text{gap}})$ , which generates a LRG between the quasi-elastically scattered projectile proton and a high mass diffractive state produced in the backward direction, is depicted in Fig. 9 (a), which corresponds to all the blocks *A*, *B*, and *C* in Fig. 8 (a)

<sup>5</sup>Strictly speaking, the two contributions to double high mass diffraction cross section, corresponding to the 1st and the last terms in the r.h.s. of Eq. (23), can not be treated separately as they correspond to the same structure of the final state. Moreover, as will be discussed in the following, the first contribution may be negative in some parts of the kinematic space; it is the sum of the two terms which provides a positively-defined result.

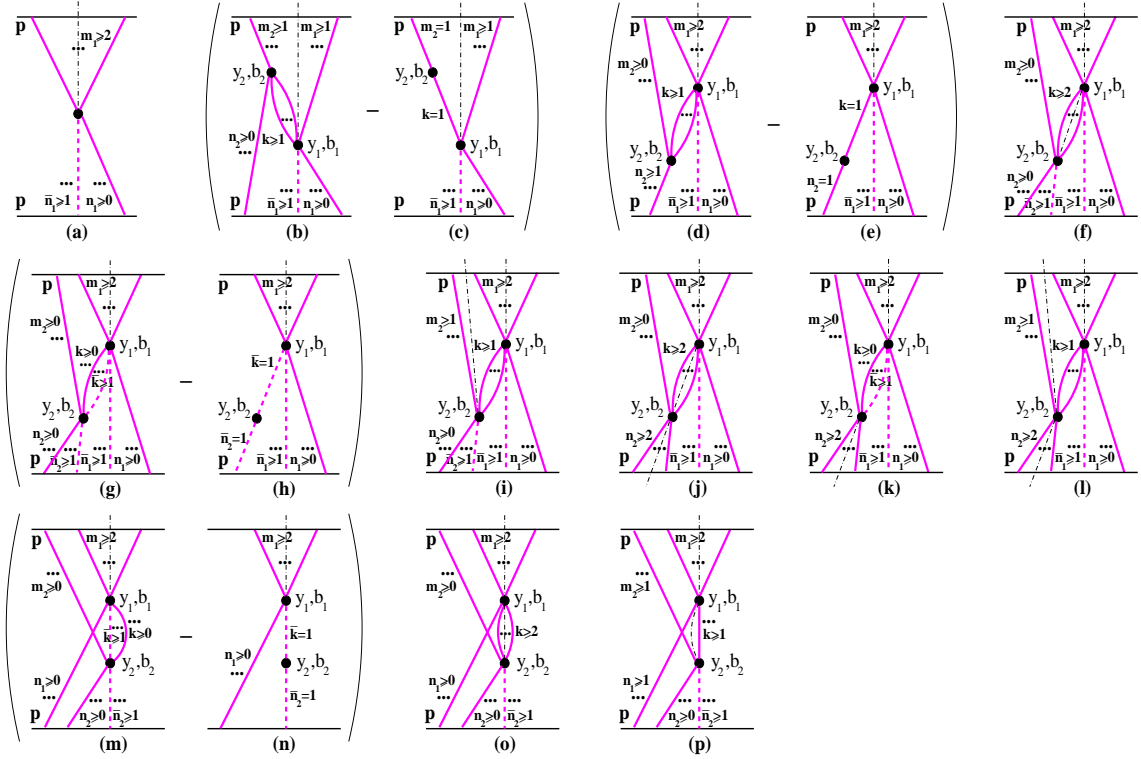


Figure 9: Simplest cut enhanced diagrams corresponding to single (target) high mass diffraction topology. Uncut and cut Pomerons are shown respectively by solid and dashed thick lines; thin dot-dashed lines indicate the position of the cut plane.

being represented by multi-Pomeron exchanges between the vertex  $(y_1, \vec{b}_1)$  and the projectile/target protons, with at least one uncut, respectively cut, Pomeron per block. Thus, we have  $m_1 \geq 2$  uncut Pomerons exchanged between the vertex  $(y_1, \vec{b}_1)$  and the projectile proton, which can be positioned both to the left and to the right of the cut plane, with at least one Pomeron on either side of the cut, plus  $\bar{n}_1 \geq 1$  cut and  $n \geq 0$  uncut Pomerons exchanged between that vertex and the target proton. Applying the Reggeon diagram technique [1, 16], we obtain the well-known result [17]

$$\frac{G}{2} \int d^2 b_1 \int_{\xi}^{\min(Y-y_{\text{gap}}, Y-\xi)} dy_1 \left[ 1 - e^{-\chi_{j_1}^{\mathbb{P}}(Y-y_1, |\vec{b}-\vec{b}_1|)} \right] \left[ 1 - e^{-\chi_{j_2}^{\mathbb{P}}(Y-y_1, |\vec{b}-\vec{b}_1|)} \right] \left[ 1 - e^{-2\chi_k^{\mathbb{P}}(y_1, b_1)} \right]. \quad (24)$$

Due to the steep fall down of the Pomeron eikonal  $\chi_j^{\mathbb{P}}(y, b)$  for large  $b$ , at very large impact parameters (24) reduces to the usual triple-Pomeron contribution

$$G \int d^2 b_1 \int_{\xi}^{\min(Y-y_{\text{gap}}, Y-\xi)} dy_1 \chi_{j_1}^{\mathbb{P}}(Y-y_1, |\vec{b}-\vec{b}_1|) \chi_{j_2}^{\mathbb{P}}(Y-y_1, |\vec{b}-\vec{b}_1|) \chi_k^{\mathbb{P}}(y_1, b_1), \quad (25)$$

which is characterized by the diffractive mass  $M_X^2 = e^{y_1}$  distribution (due to the larger slope of the soft component, it dominates very peripheral interactions):

$$f(M_X^2) \sim (M_X^2)^{-\alpha_{\mathbb{P}}(s)}.$$

On the other hand, for central ( $b \sim 0$ ) collisions at sufficiently high energies a large contribution to the integral in (24) comes from the kinematic region where  $\chi_{j_1}^{\mathbb{P}}, \chi_{j_2}^{\mathbb{P}}, \chi_k^{\mathbb{P}}$  are all large, which leads to

$$f(M_X^2) \sim 1/M_X^2.$$

The other graphs in Fig. 9 describe absorptive corrections to the simple diagram of Fig. 9 (a). For example, the diagram in Fig. 9 (b) (minus the Pomeron self-coupling contribution of Fig. 9 (c)) corresponds to having an internal multi-Pomeron vertex in the block  $A$  or  $B$  in Fig. 8 (a). Absorptive effects arise due to additional rescatterings on the projectile (for  $m_2 \geq 2$ ) or/and on the target (for  $n_2 \geq 1$ ), or/and due to the emergence of Pomeron loops (for  $k \geq 2$ ), giving rise to the (negative) screening contribution<sup>6</sup>

$$\begin{aligned} & \frac{G^2}{2} \int d^2 b_1 d^2 b_2 \int_{\xi}^{\min(Y-y_{\text{gap}}, Y-2\xi)} dy_1 \int_{y_1+\xi}^{Y-\xi} dy_2 \left(1 - e^{-2\chi_k^{\mathbb{P}}(y_1, b_1)}\right) \\ & \times \left\{ \left(1 - e^{-\chi^{\mathbb{P}}(y_2-y_1, |\vec{b}_2-\vec{b}_1|)}\right) e^{-\chi_k^{\mathbb{P}}(y_2, b_2)} \left[ \left(1 - e^{-\chi_{j_1}^{\mathbb{P}}(Y-y_2, |\vec{b}-\vec{b}_2|)}\right) \left(1 - e^{-\chi_{j_2}^{\mathbb{P}}(Y-y_1, |\vec{b}-\vec{b}_1|)}\right) \right. \right. \\ & \times e^{-\chi_{j_1}^{\mathbb{P}}(Y-y_1, |\vec{b}-\vec{b}_1|)} + \left. \left(1 - e^{-\chi_{j_2}^{\mathbb{P}}(Y-y_2, |\vec{b}-\vec{b}_2|)}\right) \left(1 - e^{-\chi_{j_1}^{\mathbb{P}}(Y-y_1, |\vec{b}-\vec{b}_1|)}\right) e^{-\chi_{j_2}^{\mathbb{P}}(Y-y_1, |\vec{b}-\vec{b}_1|)} \right] \\ & - \chi^{\mathbb{P}}(y_2 - y_1, |\vec{b}_2 - \vec{b}_1|) \left[ \chi_{j_1}^{\mathbb{P}}(Y - y_2, |\vec{b} - \vec{b}_2|) \left(1 - e^{-\chi_{j_2}^{\mathbb{P}}(Y-y_1, |\vec{b}-\vec{b}_1|)}\right) e^{-\chi_{j_1}^{\mathbb{P}}(Y-y_1, |\vec{b}-\vec{b}_1|)} \right. \\ & \left. \left. + \chi_{j_2}^{\mathbb{P}}(Y - y_2, |\vec{b} - \vec{b}_2|) \left(1 - e^{-\chi_{j_1}^{\mathbb{P}}(Y-y_1, |\vec{b}-\vec{b}_1|)}\right) e^{-\chi_{j_2}^{\mathbb{P}}(Y-y_1, |\vec{b}-\vec{b}_1|)} \right] \right\}. \quad (26) \end{aligned}$$

In turn, the diagrams in Fig. 9 (d-p) correspond to having an internal multi-Pomeron vertex in the block  $C$  in the representation of Fig. 8 (a). One can immediately notice that the summary contribution of the graphs in Fig. 9 (d-l) is zero. Indeed, these diagrams differ by the structure of the sub-graph formed by all the Pomerons coupled to the vertex  $(y_2, \vec{b}_2)$ : while it remains uncut in Fig. 9 (d,e), it is cut in all possible ways in Fig. 9 (e-l). The  $s$ -channel unitarity assures a precise cancellation between these uncut and cut contributions, which can be also verified by an explicit calculation. Thus, non-zero corrections come only from the graphs in Fig. 9 (m-p) and read

$$\begin{aligned} & \frac{G^2}{2} \int d^2 b_1 d^2 b_2 \int_{2\xi}^{\min(Y-y_{\text{gap}}, Y-\xi)} dy_1 \int_{\xi}^{y_1-\xi} dy_2 \left(1 - e^{-\chi_{j_1}^{\mathbb{P}}(Y-y_1, |\vec{b}-\vec{b}_1|)}\right) \left(1 - e^{-\chi_{j_2}^{\mathbb{P}}(Y-y_1, |\vec{b}-\vec{b}_1|)}\right) \\ & \times \left\{ \left(1 - e^{-\chi^{\mathbb{P}}(y_1-y_2, |\vec{b}_1-\vec{b}_2|)}\right) \left(1 - e^{-2\chi_k^{\mathbb{P}}(y_2, b_2)}\right) e^{-\chi_k^{\mathbb{P}}(y_1, b_1)} \left[ e^{-\chi_{j_1}^{\mathbb{P}}(Y-y_2, |\vec{b}-\vec{b}_2|)} - \chi_{j_2}^{\mathbb{P}}(Y-y_2, |\vec{b}-\vec{b}_2|) \right. \right. \\ & \left. \left. - \left( e^{-\chi_{j_1}^{\mathbb{P}}(Y-y_2, |\vec{b}-\vec{b}_2|)} + e^{-\chi_{j_2}^{\mathbb{P}}(Y-y_2, |\vec{b}-\vec{b}_2|)} \right) \left(1 - e^{-\chi_k^{\mathbb{P}}(y_1, b_1)}\right) \right] \right. \\ & \left. - 2\chi^{\mathbb{P}}(y_1 - y_2, |\vec{b}_1 - \vec{b}_2|) \chi_k^{\mathbb{P}}(y_2, b_2) e^{-2\chi_k^{\mathbb{P}}(y_1, b_1)} \right\}. \quad (27) \end{aligned}$$

It is noteworthy that at small impact parameters the integrands in (26), (27) are damped by the exponential factors  $\exp(-\chi_{j_{1/2}}^{\mathbb{P}}(Y-y_1, |\vec{b}-\vec{b}_1|))$  and  $\exp(-\chi_k^{\mathbb{P}}(y_1, b_1))$  correspondingly, as noted in [5, 6], while in very peripheral interactions these contributions are suppressed by an additional power of the triple-Pomeron coupling, compared to the lowest order result, Eq. (24). However, in the intermediate range they give rise to very important absorptive effects. Let us also remark that in the graphs in Fig. 9 (o,p) there is just a narrow bunch of particles produced at  $y \sim y_1$ , which results from the cut multi-Pomeron vertex  $(y_1, \vec{b}_1)$ . Such low mass diffractive states produced at central rapidities are difficult to detect experimentally. Therefore, in the next Section we compare diffractive cross sections as calculated taking such low mass states into account or neglecting them. In the latter case, the limits for the  $y$ -integrations for these diagrams should be chosen as  $2\xi < y_1 < Y - \xi$ ,  $\xi < y_2 < \min(Y - y_{\text{gap}}, y_1 - \xi)$  (c.f. (27)).

Restricting oneself with enhanced diagrams of the lowest two orders, the contribution to  $2\chi_{j_1 j_2 k_1 k_2}^{2-\text{gap}}(Y, b, y_{\text{gap}}^{(f)}, y_{\text{gap}}^{(b)})$ , corresponding to central high mass diffraction topology, comes from the graph in Fig. 10 (h) only, which gives

<sup>6</sup>When calculating the contributions of the graphs in Fig. 9 (b,c), we take into account that the uncut multi-Pomeron vertex  $(y_2, \vec{b}_2)$ , along with the uncut Pomerons coupled to it, may be positioned on either side of the cut plane, and so do  $m_1 \geq 1$  uncut Pomerons connected to the vertex  $(y_1, \vec{b}_1)$ , such that at least one of the  $m_1$  Pomerons is positioned on the opposite side of the cut with respect to the vertex  $(y_2, \vec{b}_2)$ . More details on the calculation technique can be found in the preceding publications [11, 12].

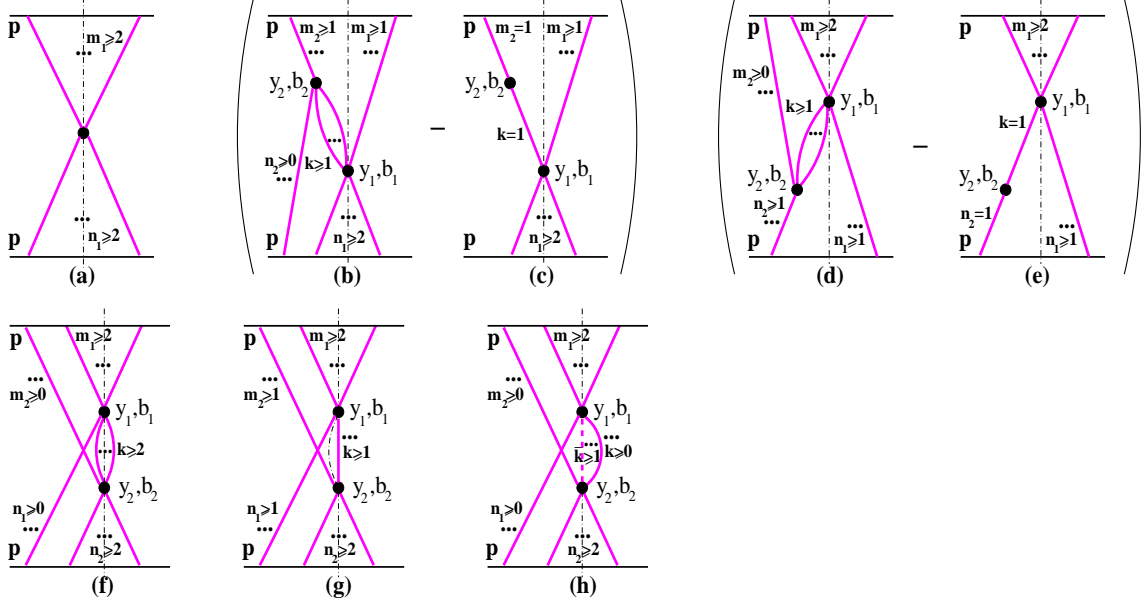


Figure 10: Simplest cut enhanced diagrams corresponding to central diffraction (DPE) topology.

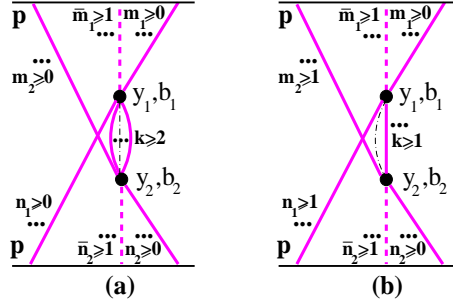


Figure 11: Simplest cut enhanced diagrams corresponding to double high mass diffraction topology.

$$\begin{aligned}
& \frac{G^2}{4} \int d^2 b_1 d^2 b_2 \int_{\max(2\xi, y_{\text{gap}}^{(b)} + \xi)}^{\min(Y - y_{\text{gap}}^{(f)}, Y - \xi)} dy_1 \int_{\xi}^{y_1 - \xi} dy_2 \left( 1 - e^{-\chi_{j_1}^{\mathbb{P}}(Y - y_1, |\vec{b} - \vec{b}_1|)} \right) \\
& \times \left( 1 - e^{-\chi_{j_2}^{\mathbb{P}}(Y - y_1, |\vec{b} - \vec{b}_1|)} \right) \left( 1 - e^{-2\chi^{\mathbb{P}}(y_1 - y_2, |\vec{b}_1 - \vec{b}_2|)} \right) \left( 1 - e^{-\chi_{k_1}^{\mathbb{P}}(y_2, b_2)} \right) \left( 1 - e^{-\chi_{k_2}^{\mathbb{P}}(y_2, b_2)} \right) \\
& \times e^{-\chi_{j_1}^{\mathbb{P}}(Y - y_2, |\vec{b} - \vec{b}_2|) - \chi_{j_2}^{\mathbb{P}}(Y - y_2, |\vec{b} - \vec{b}_2|) - \chi_{k_1}^{\mathbb{P}}(y_1, b_1) - \chi_{k_2}^{\mathbb{P}}(y_1, b_1)}. \quad (28)
\end{aligned}$$

Here again we notice a damping of the contribution at small impact parameters by the exponential factors in the 3rd line of Eq. (28). Accounting for diffractive production of narrow bunches of secondary particles at central rapidities, we have to add also contributions of the graphs in Fig. 10 (a-g), which we omit here for brevity.

Finally, the lowest order contribution to  $2\chi_{jk}^{c\text{-gap}}(Y, b, y_{\text{gap}})$ , corresponding to double high mass diffraction and a central LRG, is given by the graphs in Fig. 11 and reads

$$\begin{aligned}
& \frac{G^2}{4} \int d^2 b_1 d^2 b_2 \int_{\max(\xi + y_{\text{gap}}, 2\xi)}^{Y - \xi} dy_1 \int_{\xi}^{y_1 - \max(y_{\text{gap}}, \xi)} dy_2 \left[ \left( 1 - e^{-\chi^{\mathbb{P}}(y_1 - y_2, |\vec{b}_1 - \vec{b}_2|)} \right)^2 \right. \\
& \times e^{-\chi_j^{\mathbb{P}}(Y - y_2, |\vec{b} - \vec{b}_2|) - \chi_k^{\mathbb{P}}(y_1, b_1)} - 2 \left( 1 - e^{-\chi^{\mathbb{P}}(y_1 - y_2, |\vec{b}_1 - \vec{b}_2|)} \right) \left( 1 - e^{-\chi_j^{\mathbb{P}}(Y - y_2, |\vec{b} - \vec{b}_2|)} \right)
\end{aligned}$$

	$\alpha_{\mathbb{P}(s)}$	$\alpha_{\mathbb{P}(h)}$	$\alpha'_{\mathbb{P}(s)},$ GeV <sup>-2</sup>	$\alpha'_{\mathbb{P}(h)},$ GeV <sup>-2</sup>	$\gamma,$ GeV <sup>-1</sup>	$\eta$	$r_{h/s}$	$\Lambda_1,$ GeV <sup>-2</sup>	$\Lambda_2,$ GeV <sup>-2</sup>	$r_{3\mathbb{P}},$ GeV <sup>-1</sup>	$\gamma_{\mathbb{P}},$ GeV <sup>-1</sup>
Set (A)	1.145	1.35	0.13	0.075	1.65	0.6	0.06	1.06	0.3	0.14	0.5
Set (B)	1.15	1.35	0.165	0.08	1.75	0.6	0.065	1.03	0.3	0.15	0.5
Set (C)	1.14	1.31	0.14	0.085	1.6	0.5	0.09	1.1	0.4	0.14	0.5

Table 1: Model parameters.

$$\times \left(1 - e^{-\chi_k^{\mathbb{P}}(y_1, b_1)}\right) \left] e^{-\chi_j^{\mathbb{P}}(Y-y_2, |\vec{b}-\vec{b}_2|) - \chi_k^{\mathbb{P}}(y_1, b_1)} \left(1 - e^{-2\chi_j^{\mathbb{P}}(Y-y_1, |\vec{b}-\vec{b}_1|)}\right) \left(1 - e^{-2\chi_k^{\mathbb{P}}(y_2, b_2)}\right). \quad (29)$$

It is easy to see that the expression in the square brackets is not positively defined: for  $b \sim b_1 \sim b_2 \sim 0$  the first term is strongly damped by the exponential factor  $e^{-\chi_k^{\mathbb{P}}(Y-y_2, |\vec{b}-\vec{b}_2|) - \chi_k^{\mathbb{P}}(y_1, b_1)}$ . Thus, for  $b \sim 0$  the whole expression (29) may provide a negative result. It is the complete contribution to the double high mass diffraction cross section, given by the sum of the first and the last terms in the r.h.s. of Eq. (23), which has the positive definiteness due to the dominance of the second contribution in the small  $b$  region. In fact, the diagram in Fig. 11 (b) describes the interference between the amplitudes corresponding to a single double high mass diffraction process of Fig. 11 (a) and to a superposition of two (projectile and target) single high mass diffraction processes of Fig. 9 (a).

## 4 Numerical results

The parameters for the above-described model approach have been fixed to reproduce the available data on total, elastic, and diffractive proton-proton cross sections, the elastic scattering slope, and the differential elastic cross section. As the numerical calculations proved to be rather time-consuming and some experimental results do not agree well with each other, we did not perform a standard  $\chi^2$  minimization procedure but rather tuned the parameters to obtain an overall acceptable description of the data points.

In order to reduce the number of adjustable parameters, we used equal weights for elastic scattering eigenstates,  $C_1 = C_2 = 1/2$ . On the other hand, due to a rather weak dependence of the results on the  $\gamma_{\mathbb{P}}$  parameter (Eq. (11)), within certain limits, we used a fixed value  $\gamma_{\mathbb{P}} = 0.5 \text{ GeV}^{-1}$ . The latter point requires a special discussion. As shown in [10], the above-described resummation scheme approaches in the “dense” limit ( $s \rightarrow \infty, b \rightarrow 0$ ) the asymptotic result obtained in [6], which corresponds to a multi-channel non-enhanced eikonal scheme based on a “renormalized” Pomeron, with the intercept

$$\alpha_{\mathbb{P}}^{\text{ren}} = \alpha_{\mathbb{P}} - r_{3\mathbb{P}}/\gamma_{\mathbb{P}}. \quad (30)$$

Considering a single Pomeron pole contribution to  $D^{\mathbb{P}}(s, t)$ , the consistency requires that the renormalized Pomeron remains an overcritical one, i.e.  $\alpha_{\mathbb{P}}^{\text{ren}} > 1$ , in order to preserve the energy rise of total cross section. Here, using two Pomeron poles, we investigate a more interesting option, choosing  $\gamma_{\mathbb{P}}$  such that the renormalized soft Pomeron becomes an undercritical one,  $\alpha_{\mathbb{P}(s)}^{\text{ren}} < 1$ , corresponding to the saturation of the soft physics, while the hard Pomeron remains an overcritical one after the renormalization,  $\alpha_{\mathbb{P}(h)}^{\text{ren}} > 1$ . This corresponds to the picture where central hadronic collisions are dominated in the very high energy limit by cascades of harder partons, while peripheral interactions remain governed by soft parton cascades.

All other model parameters have been tuned for two choices on the Pomeron mass cutoff,  $\xi = 2$  and 1.5, fitting the CDF value  $\sigma^{\text{tot}} = 80.03 \pm 2.24 \text{ mb}$  [18] at the Tevatron, or using  $\xi = 2$  and fitting the E710 value  $\sigma^{\text{tot}} = 72.8 \pm 3.1 \text{ mb}$  [19]. The three parameter sets, referred to as (A), (B), and (C) in the following, are listed in Table 1, with the vertex factors  $\gamma_i$  being expressed as  $\gamma_{1/2} = \gamma(1 \pm \eta)$ . Surprisingly, we got relatively large slopes both for the soft and the hard Pomeron components,  $\alpha'_{\mathbb{P}(s)} \sim 0.13 \div 0.17 \text{ GeV}^{-2}$  and  $\alpha'_{\mathbb{P}(h)} \simeq 0.08 \text{ GeV}^{-2}$ , to be compared with

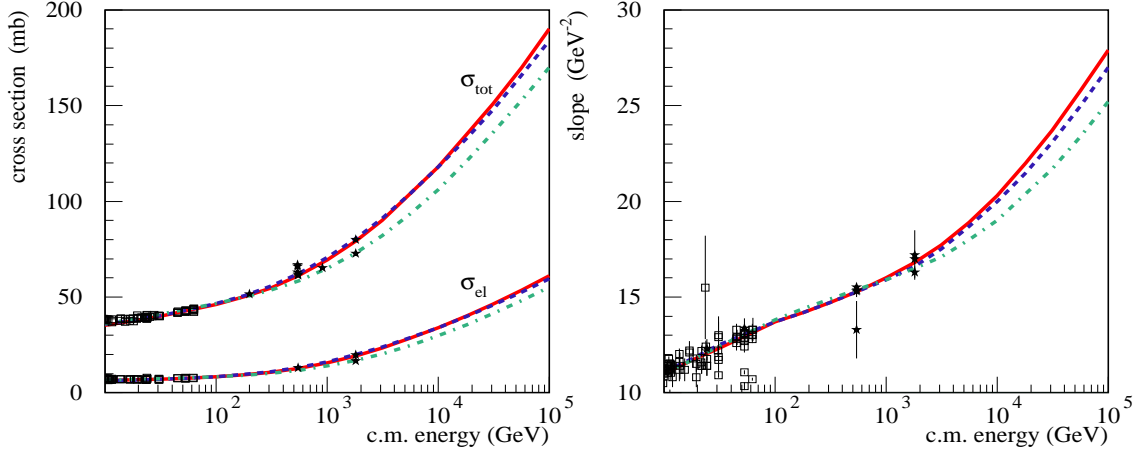


Figure 12: Total and elastic proton-proton cross sections (left) and elastic scattering slope (right) calculated using the parameter sets (A), (B), and (C) - solid, dashed and dot-dashed lines correspondingly. The compilation of data is from [20].

	$\sigma^{\text{tot}}$	$\sigma^{\text{el}}$	$\sigma^{\text{SD}}$	$\sigma^{\text{DD}}$	$\sigma_{\text{LM}}^{\text{SD}}$	$\sigma_{\text{HM}}^{\text{SD}}$	$\sigma_{\text{LM}}^{\text{DD}}$	$\sigma_{\text{HM}}^{\text{DD}}$	$\sigma_{\text{LHM}}^{\text{DD}}$	$\sigma^{\text{DPE}}$
Set (A)	61.0	12.7	8.79	2.84	3.80	5.00 (4.82)	0.31	1.40	1.13 (1.08)	0.24 (0.07)
Set (B)	62.1	13.2	8.85	3.32	3.76	5.08 (4.94)	0.30	1.92	1.11 (1.07)	0.26 (0.11)
Set (C)	58.4	11.7	9.08	2.91	2.60	6.48 (6.26)	0.14	1.81	0.95 (0.92)	0.33 (0.09)

Table 2: Calculated total, elastic, and diffractive proton-proton cross sections (in mb) for  $\sqrt{s} = 546$  GeV.

$\alpha'_p \simeq 0.05 \text{ GeV}^{-2}$  in [7] and  $\alpha'_p \simeq 0.01 \text{ GeV}^{-2}$  in [9]. On the other hand, the obtained values for the triple-Pomeron coupling are close to the old estimates [6, 14].

The results of the calculations for total and elastic proton-proton cross sections and for the forward elastic scattering slope, using the three parameter sets obtained, are plotted in Fig. 12 in comparison with experimental data. The calculated differential elastic cross sections are presented in Fig. 13. And in Fig. 14 (left) we show, in comparison with CDF measurements [21, 22], single diffraction cross section  $\sigma^{\text{SD}}$  for diffractive mass squared  $M_X^2 < 0.15 s$  and double diffraction cross section  $\sigma^{\text{DD}}(y_{\text{gap}}^{(0)} \geq 3)$  corresponding to a central rapidity gap of size  $y_{\text{gap}} \geq 3$ , which spans the central rapidity  $y = Y/2$  point. In addition, in Fig. 14 (right) we plot partial contributions to  $\sigma^{\text{SD}}$  and  $\sigma^{\text{DD}}(y_{\text{gap}}^{(0)} \geq 3)$  from correspondingly single and double low ( $\sigma_{\text{LM}}^{\text{SD}}, \sigma_{\text{LM}}^{\text{DD}}$ ) and high ( $\sigma_{\text{HM}}^{\text{SD}}, \sigma_{\text{HM}}^{\text{DD}}$ ) mass diffraction, and a contribution  $\sigma_{\text{LHM}}^{\text{DD}}$  to  $\sigma^{\text{DD}}(y_{\text{gap}}^{(0)} \geq 3)$  from the process corresponding to a high mass diffraction of one hadron and a low mass excitation of the other one. The numerical values for  $\sigma^{\text{tot}}, \sigma^{\text{el}}, \sigma^{\text{SD}}, \sigma^{\text{DD}}$ , central diffraction cross section  $\sigma^{\text{DPE}}$ , and for partial contributions to low and high mass diffraction cross sections  $\sigma_{\text{LM}}^{\text{SD/DD}}, \sigma_{\text{HM}}^{\text{SD/DD}}, \sigma_{\text{LHM}}^{\text{DD}}$  for the CERN SPS, Tevatron, and LHC energies are given in Tables 2, 3, 4 correspondingly, with the diffraction cross sections now being calculated for the minimal allowed rapidity gap size  $y_{\text{gap}} = \xi$ . The values in brackets for  $\sigma_{\text{HM}}^{\text{SD}}, \sigma_{\text{LHM}}^{\text{DD}}$ , and  $\sigma^{\text{DPE}}$  in Tables 2, 3, 4 are obtained if the contributions of low mass diffractive states produced at central rapidities are neglected.

Clearly, both the model parameters and the cross section results depend rather weakly on the choice of the Pomeron mass cutoff. The obtained diffractive cross sections appeared to be rather insensitive to whether or not low mass diffractive states produced at central rapidities are taken into account, with the exception of  $\sigma^{\text{DPE}}$  which is dominated by such contributions, more precisely, by the one of the graph in Fig. 24 (c), Eq. (53). The observed high energy rise of total and elastic



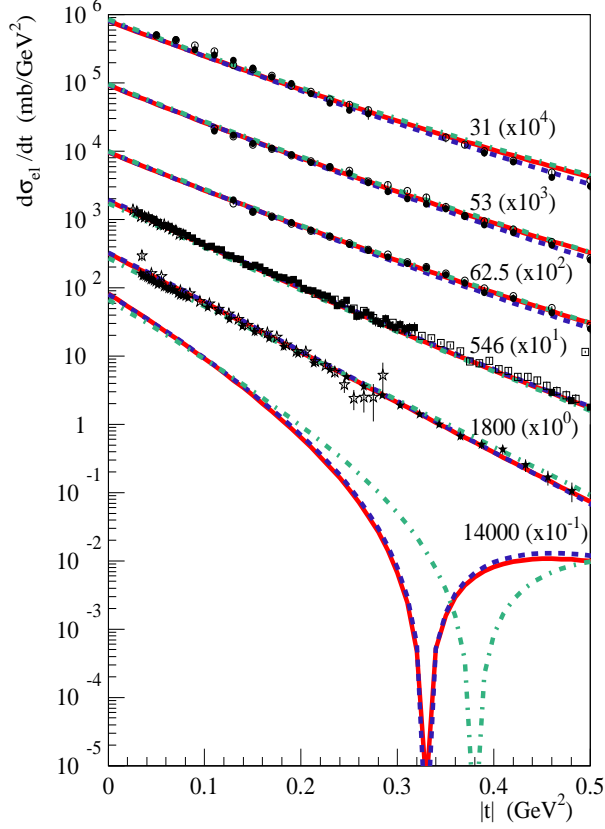


Figure 13: Calculated differential elastic proton-proton cross section for different  $\sqrt{s}$  in GeV (as indicated in the plot) compared to experimental data [23, 24, 25, 26, 27]. The meaning of the lines is the same as in Fig. 12.

	$\sigma^{\text{tot}}$	$\sigma^{\text{el}}$	$\sigma^{\text{SD}}$	$\sigma^{\text{DD}}$	$\sigma_{\text{LM}}^{\text{SD}}$	$\sigma_{\text{HM}}^{\text{SD}}$	$\sigma_{\text{LM}}^{\text{DD}}$	$\sigma_{\text{HM}}^{\text{DD}}$	$\sigma_{\text{LHM}}^{\text{DD}}$	$\sigma^{\text{DPE}}$
Set (A)	79.3	19.3	9.62	3.62	5.10	4.52 (4.38)	0.48	1.95	1.20 (1.17)	0.19 (0.08)
Set (B)	80.5	19.9	9.84	4.06	5.08	4.78 (4.66)	0.45	2.37	1.24 (1.20)	0.23 (0.11)
Set (C)	73.0	16.8	9.60	3.93	3.40	6.20 (6.04)	0.19	2.70	1.04 (1.01)	0.31 (0.12)
Ref. [7]	73.7	16.4	13.8		4.1	9.7				
Ref. [9]	73.3	16.3	9.76	5.36	8.56	1.2				

Table 3: Same as in Table 2 for  $\sqrt{s} = 1.8$  TeV.

cross sections is qualitatively similar for all the three parameter sets, with  $\sigma^{\text{tot}}$  reaching  $114 \div 128$  mb at the LHC. This appears to be quite different to the results of [7] and [9], where a much flatter high energy behavior of  $\sigma^{\text{tot}}$  and  $\sigma^{\text{el}}$  has been predicted, with the total cross section value of 92 mb only at  $\sqrt{s} = 14$  TeV and the elastic one being almost a factor of two smaller compared to our results with the parameter sets (A) and (B).<sup>7</sup> The calculated differential elastic cross section at  $\sqrt{s} = 14$  TeV manifests a diffractive peak at  $-t \simeq 3.3$  GeV<sup>2</sup> for the parameter sets (A) and (B), which is shifted towards  $-t \simeq 3.8$  GeV<sup>2</sup> for the set (C).

It is interesting to compare the high energy behavior of partial contributions to  $\sigma^{\text{SD}}$  from low and high mass diffractive processes - see Fig. 14 (right) and Tables 2, 3, 4. While the high

<sup>7</sup>Possible causes for these discrepancies will be analyzed in the next Section.



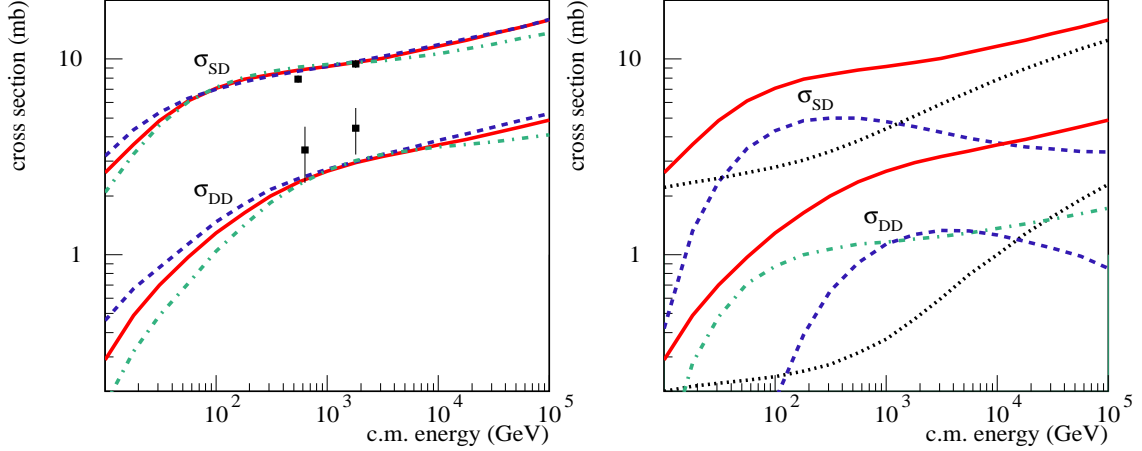


Figure 14: Left: single and double diffraction proton-proton cross sections ( $\sigma^{\text{SD}}(M_X^2/s < 0.15)$ ,  $\sigma^{\text{DD}}(y_{\text{gap}}^{(0)} \geq 3)$ ), as calculated using the parameter sets (A), (B), and (C) - solid, dashed and dot-dashed lines correspondingly, compared to CDF data [21, 22]. Right:  $\sigma^{\text{SD}}(M_X^2/s < 0.15)$  and  $\sigma^{\text{DD}}(y_{\text{gap}}^{(0)} \geq 3)$  calculated using the parameter set (A) - solid lines, partial contributions of high and low mass diffraction:  $\sigma_{\text{HM}}^{\text{SD/DD}}$  and  $\sigma_{\text{LM}}^{\text{SD/DD}}$  - dashed and dotted lines correspondingly,  $\sigma_{\text{LHM}}^{\text{DD}}$  - dot-dashed line.

	$\sigma^{\text{tot}}$	$\sigma^{\text{el}}$	$\sigma^{\text{SD}}$	$\sigma^{\text{DD}}$	$\sigma_{\text{LM}}^{\text{SD}}$	$\sigma_{\text{HM}}^{\text{SD}}$	$\sigma_{\text{LM}}^{\text{DD}}$	$\sigma_{\text{HM}}^{\text{DD}}$	$\sigma_{\text{LHM}}^{\text{DD}}$	$\sigma^{\text{DPE}}$
Set (A)	128	37.5	12.1	4.61	8.48	3.62 (3.54)	1.15	2.06	1.40 (1.37)	0.10 (0.05)
Set (B)	126	37.3	12.4	5.18	8.22	4.24 (4.14)	1.08	2.50	1.60 (1.56)	0.14 (0.07)
Set (C)	114	33.0	11.0	4.83	5.76	5.22 (5.12)	0.47	3.15	1.22 (1.19)	0.19 (0.09)
Ref. [7]	91.7	21.5	19.0		4.9	14.1				
Ref. [9]	92.1	20.9	11.8	6.08	10.5	1.28				

Table 4: Same as in Table 2 for  $\sqrt{s} = 14$  TeV.

energy trend of  $\sigma_{\text{LM}}^{\text{SD}}$  resembles, as it should, the one of  $\sigma^{\text{el}}$  (c.f. Eqs. (6) and (8)),  $\sigma_{\text{HM}}^{\text{SD}}$  reaches its maximal values well below the LHC and slowly dies out in the very high energy asymptotics. Such a tendency is well expected, as the interaction approaches the black disk limit at  $s \rightarrow \infty$ ; the calculated ratios  $\sigma^{\text{el}}/\sigma^{\text{tot}}$  rise from  $0.20 \div 0.21$  to  $0.29 \div 0.30$  in the c.m. energy range between 546 GeV and 14 TeV. The probability for a rapidity gap not to be covered by secondary particles produced in additional inelastic rescattering processes becomes negligible at not too large impact parameters; the diffractive configurations of final states can thus survive in very peripheral collisions only. This tendency is supported by the results in Tables 2, 3, 4: using the parameter set (C) which corresponds to slightly smaller  $\sigma^{\text{el}}/\sigma^{\text{tot}}$  ratios, we obtained bigger values for  $\sigma_{\text{HM}}^{\text{SD}}$ . However, apart from this well-known eikonal rapidity gap suppression described by the RGS factor  $S_{j_1 j_2 k k}$  (Eqs. (20-21)), the observed high energy trend of  $\sigma_{\text{HM}}^{\text{SD}}$  is the consequence of the unitarization of the contribution  $2\chi_{j_1 j_2 k}^{1-\text{gap}}(Y, b, y_{\text{gap}})$  of the irreducible diffractively cut graph itself. It is worth stressing that the results depend crucially on whether the corresponding absorptive corrections are properly resummed.

To illustrate this point, we calculated single high mass diffraction cross sections for the parameter set (A) using Eq. (20), taking into account all enhanced diagram contributions to elastic scattering amplitude (i.e. using  $\chi_{jk}^{\text{enh}}$  as defined by Eq. (19)) but employing partial resummations for the contribution  $2\chi_{j_1 j_2 k}^{1-\text{gap}}(Y, b, y_{\text{gap}})$ : i) as defined by the contributions of the graphs in Fig. 23 (a,b), given in Eq. (52); ii) keeping only the lowest order result of Fig. 9 (a) - Eq. (24); iii) restricting

ourselves with the triple-Pomeron contribution of Eq. (25). The obtained high energy behavior of  $\sigma_{\text{HM}}^{\text{SD}}(s)$  is plotted in Fig. 15 (left) in comparison with the full resummation result. In addition,

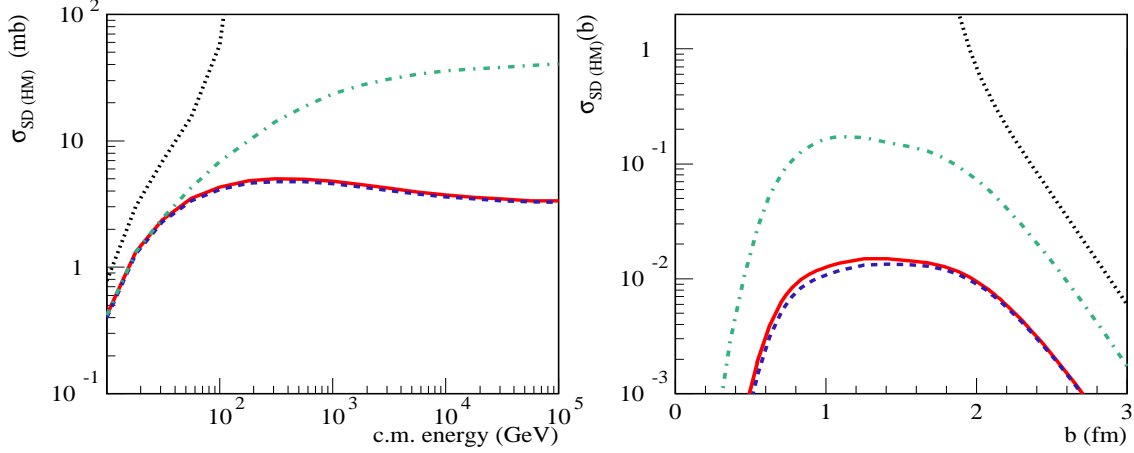


Figure 15: High energy behavior of  $\sigma_{\text{HM}}^{\text{SD}}$  (left) and single high mass diffraction profile at  $\sqrt{s} = 14$  TeV (right) as calculated using the full resummation scheme, taking into account the contributions of the graphs in Fig. 23 (a,b), using the lowest order result of Fig. 9 (a), or keeping only the triple-Pomeron contribution to  $2\chi_{j_1 j_2 k}^{1-\text{gap}}(Y, b, y_{\text{gap}})$  - solid, dashed, dot-dashed, and dotted lines correspondingly (all for the parameter set (A)).

in Fig. 15 (right) we plot the corresponding profile functions  $\sigma_{\text{HM}}^{\text{SD}}(s, b)$  for  $\sqrt{s} = 14$  TeV. While restricting oneself with the contribution of the graphs in Fig. 23 (a,b) to  $2\chi_{j_1 j_2 k}^{1-\text{gap}}(Y, b, y_{\text{gap}})$  is a fairly good approximation, the corresponding values of  $\sigma_{\text{HM}}^{\text{SD}}$  being less than 5% different from the full resummation results, the other two options considered prove to be very crude. In particular, considering the triple-Pomeron contribution only, one violates the  $s$ -channel unitarity: the high mass diffraction profile function exceeds unity at small  $b$  and  $\sigma_{\text{HM}}^{\text{SD}}(s)$  increases more rapidly at  $s \rightarrow \infty$  than the total cross section.

In view of partial resummations of selected classes of enhanced diagrams in [7, 9], it is interesting to investigate the relative importance of net-like and loop-like enhanced graphs. Restricting ourselves with the net-like contributions and neglecting Pomeron loops would bring us back to the approach of Ref. [10]. In such a case, the contribution to elastic scattering amplitude of all irreducible enhanced diagrams  $\chi_{jk}^{\text{enh}}$  is given by Eq. (19), with the net-fan eikonal  $\chi_{jk}^{\text{net}}$  being defined in Eq. (16), under the replacements  $1 - e^{-\chi^{\text{loop}}} \rightarrow \chi^{\text{p}}$ ,  $\chi_j^{\text{loop}} \rightarrow \chi_j^{\text{p}}$ ,  $\chi_j^{\text{loop}(1)} \rightarrow \chi_j^{\text{p}}$  in both equations. On the other hand, taking into account Pomeron loop diagrams only, we just have to keep the contributions of the last two graphs in Fig. 6, i.e. to retain just the term in the 4th line of Eq. (19) in the integrand in the r.h.s. of the equation. The obtained energy dependencies of  $\sigma^{\text{tot}}$  and  $\sigma^{\text{el}}$  are compared in Fig. 16 with the full resummation results. It is easy to see that both classes considered of enhanced diagrams provide important absorptive corrections and none of them can be neglected in the high energy limit. Still, taking into consideration net-like graphs only, the calculated cross sections come somewhat closer to the ones obtained using the complete treatment. This is due to the fact that contributions of Pomeron loops, when added to such a scheme, are damped at small impact parameters by exponential factors, as noticed already in [5, 6] (such a suppression has been discussed in Section 3.2 for particular examples of diffractively cut graphs), while at large  $b$  they are suppressed by additional powers of the small triple-Pomeron coupling.<sup>8</sup> On the other hand,

<sup>8</sup>In general, relative importance of Pomeron loop corrections depends on the parameters of the scheme, primarily, on the Pomeron slope and on the value of the vertex parameter  $\gamma_{\text{p}}$  (see Eq. (11)). For smaller  $\alpha'_{\text{p}}$ , the smallness of the triple-Pomeron coupling  $r_{3\text{p}}$  is compensated at large impact parameters by the factor  $1/\alpha'_{\text{p}}$ . On the other hand,

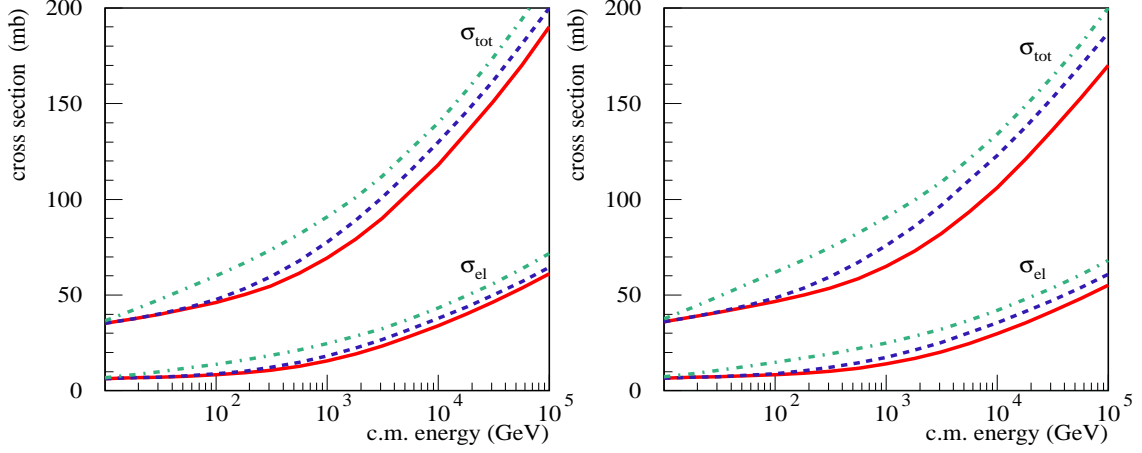


Figure 16: Total and elastic proton-proton cross sections based on the resummation of all significant enhanced diagram contributions (solid lines), on the resummation of net-like enhanced graphs (dashed lines), or taking into account Pomeron loop diagrams only (dot-dashed lines), as calculated using the parameter set (A) – left and (C) – right.

the resummation of just Pomeron loop graphs is far insufficient for cross section calculations.

From the discussion above, one may expect that corrections due to additional loop-like graphs of the kinds depicted in Fig. 7, which are neglected in the present treatment, are sufficiently small. To verify that, we calculated simplest contributions of both kinds to elastic scattering amplitude. First, we enlarged the set of graphs corresponding to irreducible 2-point sequences of Pomerons and Pomeron loops by adding the diagram of Fig. 17 (a), where we consider any number ( $\geq 1$ )

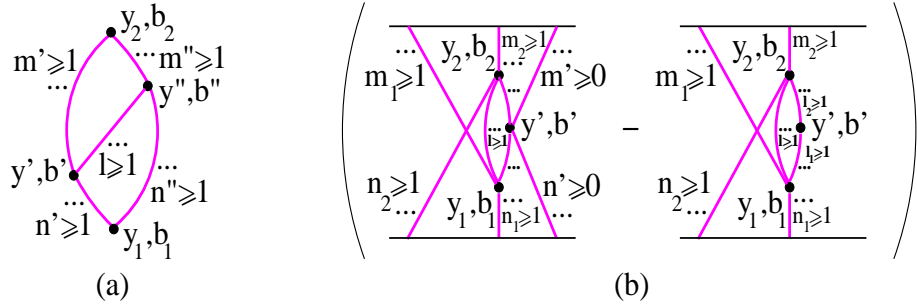


Figure 17: Considered corrections to the loop sequence contribution  $\Delta\chi^{\text{loop}}$  (a) and to the total eikonal  $\Delta\chi_{jk}^{\text{enh}}$  (b).

of Pomerons exchanged between the vertices  $(y_1, \vec{b}_1)$  and  $(y', \vec{b}')$ ,  $(y_1, \vec{b}_1)$  and  $(y'', \vec{b}'')$ ,  $(y', \vec{b}')$  and  $(y'', \vec{b}'')$ ,  $(y', \vec{b}')$  and  $(y_2, \vec{b}_2)$ ,  $(y'', \vec{b}'')$  and  $(y_2, \vec{b}_2)$ , which resulted in a modification

$$\chi^{\text{loop}}(y_1 - y_2, |\vec{b}_1 - \vec{b}_2|) \rightarrow \chi^{\text{loop}}(y_1 - y_2, |\vec{b}_1 - \vec{b}_2|) + \Delta\chi^{\text{loop}}(y_1 - y_2, |\vec{b}_1 - \vec{b}_2|),$$

where

$$\Delta\chi^{\text{loop}}(y_1 - y_2, |\vec{b}_1 - \vec{b}_2|) = G \int_{y_1+\xi}^{y_2-2\xi} dy' \int_{y'+\xi}^{y_2-\xi} dy'' \int d^2b' d^2b'' \left[ 1 - e^{-\chi^{\text{P}}(y''-y', |\vec{b}''-\vec{b}'|)} \right]$$

with  $\gamma_{\text{P}} \rightarrow 0$  the eikonal suppression of loop contributions vanishes. However, as discussed above, the consistency requirement severely restricts the possible range of  $\gamma_{\text{P}}$  values:  $\gamma_{\text{P}} > r_{3\text{P}}/\Delta$  (see Eq. (30)).

$$\times \left[ 1 - e^{-\chi^{\mathbb{P}}(y'-y_1, |\vec{b}'-\vec{b}_1|)} \right] \left[ 1 - e^{-\chi^{\mathbb{P}}(y''-y_1, |\vec{b}''-\vec{b}_1|)} \right] \left[ 1 - e^{-\chi^{\mathbb{P}}(y_2-y', |\vec{b}_2-\vec{b}'|)} \right] \left[ 1 - e^{-\chi^{\mathbb{P}}(y_2-y'', |\vec{b}_2-\vec{b}''|)} \right].$$

The so-redefined loop contributions have been used in (16) and (19) to calculate the eikonals  $\chi_{jk}^{\text{net}}$  and  $\chi_{jk}^{\text{enh}}$ , the latter being then applied for cross section calculations. Alternatively, we added the contribution of the graphs of Fig. 17 (b), where the surface of the loop is coupled to the projectile or/and target protons by additional Pomeron exchanges, directly to the eikonal  $\chi_{jk}^{\text{enh}}$ , i.e.

$$\chi_{jk}^{\text{enh}}(s, b) \rightarrow \chi_{jk}^{\text{enh}}(s, b) + \Delta\chi_{jk}^{\text{enh}}(s, b),$$

with

$$\begin{aligned} \Delta\chi_{jk}^{\text{enh}}(s, b) = & G \int_{\xi}^{Y-3\xi} dy_1 \int_{y_1+2\xi}^{Y-\xi} dy_2 \int_{y_1+\xi}^{y_2-\xi} dy' \int d^2b_1 d^2b_2 d^2b' \left[ 1 - e^{-\chi_j^{\mathbb{P}}(Y-y_2, |\vec{b}-\vec{b}_2|)} \right] \\ & \times \left[ 1 - e^{-\chi_k^{\mathbb{P}}(y_1, b_1)} \right] e^{-\chi_j^{\mathbb{P}}(Y-y_1, |\vec{b}-\vec{b}_1|) - \chi_k^{\mathbb{P}}(y_2, b_2)} \left[ 1 - e^{-\chi^{\mathbb{P}}(y_2-y_1, |\vec{b}_2-\vec{b}_1|)} \right] \left[ 1 - e^{-\chi^{\mathbb{P}}(y_2-y', |\vec{b}_2-\vec{b}'|)} \right] \\ & \times \left[ 1 - e^{-\chi^{\mathbb{P}}(y'-y_1, |\vec{b}'-\vec{b}_1|)} \right] \left[ 1 - e^{-\chi_j^{\mathbb{P}}(Y-y', |\vec{b}-\vec{b}'|) - \chi_k^{\mathbb{P}}(y', b')} \right]. \end{aligned}$$

In both cases, we did not observe any changes for the computed cross sections within the calculation accuracy (few per mille).

## 5 Discussion of other approaches

In order to understand the differences of our treatment compared to other approaches we are going to analyze the latter in some detail. We shall mainly concentrate of the formalism of Ref. [7], which is to some extent similar to our treatment of Ref. [10] in the sense that one takes into account multi-Pomeron vertices  $G^{(m,n)}$  for arbitrary  $m, n$  ( $m+n \geq 3$ ) and performs resummation of net-like enhanced graphs (without Pomeron loops). The peculiarity of the treatment of Ref. [7] is that assuming the vertices  $G^{(m,n)}$  to be of the form

$$G^{(m,n)} \sim n m \lambda^{m+n-2}, \quad (31)$$

the  $m$  (respectively  $n$ ) Pomerons entering the vertex from the projectile (target) side are no longer identical to each other, as was the case in (11). Instead, there is one “more equal” Pomeron above and one below the vertex, which represent the “main scattering” process, while other Pomerons are related to absorptive corrections. Thus, an arbitrary irreducible enhanced graph has a structure which is exemplified in Fig. 18. The main scattering process is formed by the sequence of Pomerons

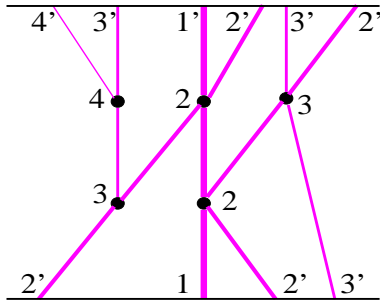


Figure 18: The structure of enhanced net-like graphs, corresponding to the parametrization (31) of multi-Pomeron vertices.

shown symbolically by the thickest lines, marked (11’). Additional rescatterings are described by

Pomeron sequences drawn as less thick lines, marked (22'). Those in turn undergo additional rescatterings marked (33'), etc. This allows one to calculate the opacity for proton-proton scattering  $\Omega_{jk}(s, b)$  (Eq. (10)) as a convolution of two ‘‘parton opacities’’, which are ‘‘glued’’ together at some rapidity  $y$  [7]:

$$\Omega_{jk}(s, b) = \frac{1}{8\pi} \int d^2 b' \Omega_{j(k)}(Y - y, |\vec{b} - \vec{b}'|, Y, \vec{b}) \Omega_{k(j)}(y, \vec{b}', Y, \vec{b}). \quad (32)$$

The parton opacity  $\Omega_{j(k)}$  satisfies the recursive equation of Fig. 19, which is a particular case of

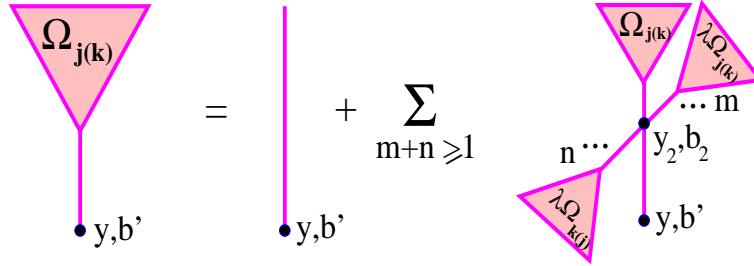


Figure 19: Recursive equation for parton opacity  $\Omega_{j(k)}(y, \vec{b}', Y, \vec{b})$ , corresponding to the parametrization (31) of multi-Pomeron vertices.

the net-fan equation (c.f. Fig. 4), corresponding to (31). Fixing the normalization in (31) by means of the triple-Pomeron coupling,  $G^{(m,n)} = r_{3\mathbb{P}}/(8\pi\lambda) n m \lambda^{m+n-2}$ , we get

$$\begin{aligned} \Omega_{j(k)}(y, \vec{b}', Y, \vec{b}) &= 2\tilde{\chi}_j^{\mathbb{P}}(y, b') + \frac{r_{3\mathbb{P}}}{\lambda} \int_{\xi}^{y-\xi} dy_2 \int d^2 b_2 \tilde{\chi}^{\mathbb{P}}(y - y_2, |\vec{b}' - \vec{b}_2|) \Omega_{j(k)}(y_2, \vec{b}_2, Y, \vec{b}) \\ &\quad \times \left\{ e^{-\frac{\lambda}{2} \Omega_{j(k)}(y_2, \vec{b}_2, Y, \vec{b}) - \frac{\lambda}{2} \Omega_{k(j)}(Y - y_2, \vec{b} - \vec{b}_2, Y, \vec{b})} - 1 \right\}, \end{aligned} \quad (33)$$

where to come to conventions of Ref. [7] we introduced the eikonals  $\tilde{\chi}_j^{\mathbb{P}}$ ,  $\tilde{\chi}^{\mathbb{P}}$  related to  $\chi_j^{\mathbb{P}}$ ,  $\chi^{\mathbb{P}}$  (see Eqs. (12-13)) as

$$\tilde{\chi}_j^{\mathbb{P}}(y, b) = \frac{\chi_j^{\mathbb{P}}(y, b)}{\gamma_{\mathbb{P}}}, \quad \tilde{\chi}^{\mathbb{P}}(y, b) = \frac{\chi^{\mathbb{P}}(y, b)}{4\pi\gamma_{\mathbb{P}}^2}. \quad (34)$$

Assuming now that the Pomeron propagator  $D^{\mathbb{P}}(s, t)$  contains a single Pomeron pole contribution and using [28]

$$\left( \frac{d}{dy} - \alpha'_{\mathbb{P}}(0) \Delta_b^{(2)} \right) \tilde{\chi}_j^{\mathbb{P}}(y, b) = \Delta \tilde{\chi}_j^{\mathbb{P}}(y, b) \quad (35)$$

(similarly for  $\tilde{\chi}^{\mathbb{P}}(y, b)$ ), with  $\Delta = \alpha_{\mathbb{P}} - 1$  and  $\Delta_b^{(2)}$  being the 2-dimensional Laplacian, we obtain

$$\begin{aligned} \left( \frac{d}{dy} - \alpha'_{\mathbb{P}}(0) \Delta_{b'}^{(2)} \right) \Omega_{j(k)}(y, \vec{b}', Y, \vec{b}) &= \Delta \Omega_{j(k)}(y, \vec{b}', Y, \vec{b}) + \frac{r_{3\mathbb{P}}}{\lambda} \int d^2 b_2 \\ &\quad \times \tilde{\chi}^{\mathbb{P}}(\xi, |\vec{b}' - \vec{b}_2|) \Omega_{j(k)}(y - \xi, \vec{b}_2, Y, \vec{b}) \left\{ e^{-\frac{\lambda}{2} \Omega_{j(k)}(y - \xi, \vec{b}_2, Y, \vec{b}) - \frac{\lambda}{2} \Omega_{k(j)}(Y - y + \xi, \vec{b} - \vec{b}_2, Y, \vec{b})} - 1 \right\}. \end{aligned} \quad (36)$$

Omitting the Pomeron mass cutoff, i.e. considering the limit  $\xi \rightarrow 0$ , and using a particular relation between  $r_{3\mathbb{P}}$ ,  $\lambda$ , and  $\Delta$

$$r_{3\mathbb{P}} = \Delta \lambda, \quad (37)$$

we obtain indeed the evolution equations for parton opacities as defined in [7]:

$$\left( \frac{d}{dy} - \alpha'_{\mathbb{P}}(0) \Delta_{b'}^{(2)} \right) \Omega_{j(k)}(y, \vec{b}', Y, \vec{b}) = \Delta \Omega_{j(k)}(y, \vec{b}', Y, \vec{b}) e^{-\frac{\lambda}{2} \Omega_{j(k)}(y, \vec{b}', Y, \vec{b}) - \frac{\lambda}{2} \Omega_{k(j)}(Y - y, \vec{b} - \vec{b}', Y, \vec{b})}. \quad (38)$$

It is worth stressing that it is the particular parametrization (31) for multi-Pomeron vertices which allowed one to obtain simple relations (32-33) between the proton-proton opacity and the net-fan contributions (parton opacities). The latter are defined with respect to some point  $(y, \vec{b}')$  which can be chosen arbitrarily on the Pomeron sequence of the “main scattering” process (marked as (11') in Fig. 18); no double counting emerges in that case. On the contrary, using the usual “symmetric” multi-Pomeron vertices (11), we had to arrange net-fans with respect to some “central” vertex  $(y_1, \vec{b}_1)$  in Fig. 6. For any enhanced graph with  $n$  internal vertices, there are  $n$  choices for the “central” vertex. Consequently, any enhanced diagram with  $n$  vertices is generated  $n$  times by the 1st graph in Fig. 6 and then subtracted  $(n - 1)$  times by the 2nd graph of the Figure.

It is noteworthy, however, that the above-discussed simplification has a price to be paid, which is the artificial hierarchy of the underlying parton cascades, depicted symbolically in Fig. 18: absorptive corrections to the main scattering process are described by parton cascades which are distinguishable from the “main stream”, with the same arrangement continued in the sub-cascades. This may happen, for example, if the main cascade is formed by harder partons (of higher virtualities), whereas additional rescatterings are dominated by softer partons. Keeping in mind that we discuss here contributions to the elastic scattering amplitude, without any “built-in trigger”, rather than to particular final states, such an hierarchy does not appear to be very natural.

The integral equation (33) for the opacity, when compared to the net-fan equation (16), helps us to understand the slower rise of  $\sigma_{pp}^{\text{tot}}$  in [7] compared to our treatment. Indeed, making replacements  $\chi_j^{\text{loop}}(y_1, b_1) \rightarrow \chi_j^{\mathbb{P}}(y_1, b_1)$ ,  $1 - e^{-\chi^{\text{loop}}(y_1 - y_2, |\vec{b}_1 - \vec{b}_2|)} \rightarrow \chi^{\mathbb{P}}(y_1 - y_2, |\vec{b}_1 - \vec{b}_2|)$  in (16) in order to suppress Pomeron loop contributions and bearing in mind the correspondence between the net-fan eikonals and the parton opacities

$$\chi_{jk}^{\text{net}}(y, \vec{b}' | Y, \vec{b}) \rightarrow \frac{\lambda}{2} \Omega_{j(k)}(y, \vec{b}', Y, \vec{b})$$

as well as the changes in the normalizations (Eq. 34), it is easy to see that for the same choice of the Pomeron propagator  $D^{\mathbb{P}}(s, t)$ , proton form factor  $F_j^{\mathbb{P}}(t)$ , triple-Pomeron coupling  $r_{3\mathbb{P}}$ , and for  $\gamma_{\mathbb{P}} = \lambda$ , Eq. (33) implies stronger screening effects compared to (16), which follows from

$$1 - e^{-\frac{\lambda}{2} \Omega_{j(k)}(y_2, \vec{b}_2, Y, \vec{b})} > \frac{\lambda}{2} \Omega_{j(k)}(y_2, \vec{b}_2, Y, \vec{b}) e^{-\frac{\lambda}{2} \Omega_{j(k)}(y_2, \vec{b}_2, Y, \vec{b})}.$$

This is, however, not the main reason for the above-mentioned difference. To understand the main cause, let us notice that in the dense limit ( $s \rightarrow \infty$ ,  $b \rightarrow 0$ ) the parton opacity  $\Omega_{j(k)}(y, \vec{b}', Y, \vec{b})$ , as defined in Eq. (33) for  $\xi = 0$ , approaches the asymptotic limit obtained in [6], which corresponds to an exchange of a single “renormalized” Pomeron between the projectile proton and the vertex  $(y, \vec{b}')$ :

$$\Omega_{j(k)}(y, \vec{b}', Y, \vec{b}) \rightarrow \tilde{\chi}_j^{\mathbb{P}\text{ren}}(y, b'), \quad (39)$$

where  $\tilde{\chi}_j^{\mathbb{P}\text{ren}}$  is defined by Eq. (12) without the  $\gamma_{\mathbb{P}}$  factor and with the renormalized Pomeron intercept

$$\alpha_{\mathbb{P}}^{\text{ren}} = \alpha_{\mathbb{P}} - r_{3\mathbb{P}}/\lambda. \quad (40)$$

To see that, it is sufficient to notice that in the discussed limit either  $\Omega_{j(k)}(y_2, \vec{b}_2, Y, \vec{b})$  or/and  $\Omega_{k(j)}(Y - y_2, \vec{b} - \vec{b}_2, Y, \vec{b})$  is large in the integrand in the r.h.s. of (12). Hence, the 1st term in the curly brackets vanishes and the equation has the solution (39). Using (37) and taking into account the relation (32) between parton opacities and the total one, we immediately observe that the approach of Ref. [7] becomes equivalent in the dense limit to a non-enhanced multi-channel eikonal scheme based on a critical Pomeron:

$$\Delta^{\text{ren}} \equiv \alpha_{\mathbb{P}}^{\text{ren}} - 1 = 0.$$

Thus, it is the particular choice (31) for multi-Pomeron vertices which is mainly responsible for the slow energy rise of  $\sigma_{pp}^{\text{tot}}$  in [7].<sup>9</sup>

On the other hand, the cross sections for diffractive processes, derived in [7] from heuristic arguments, are incompatible with the traditional RFT treatment. For example, single high mass diffraction cross section, defined as [7]<sup>10</sup>

$$\sigma_{\text{HM}}^{\text{SD}}(s) = \sum_{j,k} C_j C_k \int dy \int d^2b d^2b' \left[ 1 - e^{-\frac{\lambda}{2} \Omega_{j(k)}(Y-y, \vec{b}-\vec{b}', Y, \vec{b})} \right]^2 \Omega_{k(j)}(y, \vec{b}', Y, \vec{b}) \times \Delta e^{-\frac{\lambda}{2} \Omega_{j(k)}(Y-y, \vec{b}-\vec{b}', Y, \vec{b}) - \frac{\lambda}{2} \Omega_{k(j)}(y, \vec{b}', Y, \vec{b})} e^{-\Omega_{jk}(s,b)}, \quad (41)$$

is in variance with the old result [17] (Eq. (24)) already at the lowest order in the triple-Pomeron coupling. Indeed, keeping only single Pomeron contributions to all the opacities and omitting the RGS factor  $e^{-\Omega_{jk}(s,b)}$ , the integrand of (41) takes the form

$$\left[ 1 - e^{-\lambda \tilde{\chi}_j(Y-y, |\vec{b}-\vec{b}'|)} \right]^2 \tilde{\chi}_k(y, b') \Delta e^{-\lambda \tilde{\chi}_j(Y-y, |\vec{b}-\vec{b}'|) - \lambda \tilde{\chi}_k(y, b')}, \quad (42)$$

which is very different from the integrand in (24) for  $j_1 = j_2 = j$ . On the other hand, if we apply the AGK cutting rules to calculate the lowest order contribution of Fig. 9 (a) and use the vertices (31), we obtain, keeping the same conventions as in (42),

$$2\Delta \tilde{\chi}_j(Y-y, |\vec{b}-\vec{b}'|) \tilde{\chi}_k(y, b') \left[ 1 - e^{-\lambda \tilde{\chi}_j(Y-y, |\vec{b}-\vec{b}'|)} \right] e^{-\lambda \tilde{\chi}_j(Y-y, |\vec{b}-\vec{b}'|) - 2\lambda \tilde{\chi}_k(y, b')},$$

which is still in variance to (42). Given the importance of the proper resummation of absorptive corrections for diffractive topologies, demonstrated in the preceding Section, the different energy behavior of single high mass diffraction cross section, if calculated using Eq. (41), may not be surprising. However, the observed difference between the high energy trend of  $\sigma_{\text{HM}}^{\text{SD}}$  in [7] compared to our approach is at least partly caused by much stronger absorptive effects for parton opacities in the former case, as discussed above. The main suppression of LRG topologies is due to the eikonal RGS factor  $S_{j_1 j_2 k k}(s, b)$  (Eq. (21)) in (20) ( $e^{-\Omega_{jk}(s,b)}$  in (41)), which pushes the diffractive production away to larger and larger impact parameters with increasing energy. Using the vertices (31), one obtains a much slower energy rise of parton opacities  $\Omega_{j(k)}$ , hence, of the total opacity  $\Omega_{jk}$ , resulting in a *higher probability for a LRG to survive*. Such an assumption is supported by the much slower approach to the black disk limit in [7]. Indeed, one can see from Tables 3, 4 that in their case  $\sigma^{\text{el}}/\sigma^{\text{tot}} \simeq 0.23$  at  $\sqrt{s} = 14$  TeV, compared to our values  $\sigma^{\text{el}}/\sigma^{\text{tot}} \sim 0.29 \div 0.30$ .

Concerning the treatment of Refs. [9], we remark that the approach is based on a resummation of Pomeron loop diagrams only, which, as demonstrated in Section 4, is insufficient for cross section calculations. The contributions of net-like graphs, more precisely of *selected unitarity cuts* of fan-like diagrams, are included when calculating diffractive cross sections but neglected in the calculation of elastic scattering amplitude. In addition, the treatment takes into consideration the triple-Pomeron vertex only, neglecting other multi-Pomeron vertices  $G^{(m,n)}$  for  $m+n > 3$ . Such an approach is known to predict total cross section which becomes constant in the very high energy limit.

## 6 Outlook

In this work, we presented the first systematic analysis of the high energy behavior of total and diffractive proton-proton cross sections within the RFT framework, based on all-order resummation

<sup>9</sup>This can be seen also from Eq. (38): with the r.h.s. of the equation vanishing in the dense limit, the  $y$ -dependence of  $\Omega_{k(j)}$  comes solely from the diffusion in impact parameter space.

<sup>10</sup>Strictly speaking, Eq. (41) is designed to give the sum of the cross sections for single high mass diffraction and for double (low mass + high mass) diffraction.



of all important contributions of enhanced Pomeron diagrams. In particular, we demonstrated that absorptive corrections caused by net-like enhanced graphs and by Pomeron loop contributions are both significant and none of those classes can be neglected in the high energy limit. On the other hand, we illustrated the importance of a proper resummation of absorptive corrections for diffractively cut sub-graphs; restricting oneself with the cut triple-Pomeron diagram only, as is often done in literature, one comes into conflict with the  $s$ -channel unitarity due to the power-like energy rise of the corresponding contribution.

Compared to alternative approaches [7, 8, 9] which are based on resummations of restricted sets of enhanced diagrams, we obtained a faster energy rise of total proton-proton cross section, with our values of  $\sigma_{pp}^{\text{tot}}$  being some 25 ÷ 40% higher at the LHC energy. On the other hand, the calculated single high mass diffraction cross section reaches its maximum in the CERN SPS - Tevatron energy range and slowly decreases at higher energies, with  $\sigma_{pp}^{\text{SD}} \simeq 11 \div 12$  mb at  $\sqrt{s} = 14$  TeV. We demonstrated that the different behavior of  $\sigma_{pp}^{\text{tot}}$  and  $\sigma_{\text{HM}}^{\text{SD}}$  observed in [7], with the former reaching  $\sim 90$  mb at the LHC energy and the latter continuing to rise logarithmically up to very high energies is mainly due to the specific parametrization (31) employed for multi-Pomeron vertices, which leads to a critical Pomeron scheme in the dense limit.

Still, with our analysis based on the old RFT treatment, it bears all the drawbacks inherent to that framework: eikonal approximation which neglects energy-momentum correlations between multiple scattering processes [29], the assumption on the validity of the AGK cutting rules, in particular, that multi-Pomeron vertices remain unmodified by the cutting procedure, etc. Thus, it is up to the LHC data to decide if the described approach has something in common to the reality or is just a solution of an abstract mathematical problem.

## Acknowledgments

The author acknowledges fruitful discussions with A. Kaidalov, V. Khose, U. Maor, M. Ryskin and the support of the European Commission under the Marie Curie IEF program (grant 220251).

## Appendix

In the following, we are going to derive contributions of unitarity cuts of elastic scattering diagrams, which correspond to various diffractive topologies of hadronic final states, as depicted in Fig. 8, with single or multiple rapidity gaps not covered by secondary particle production. The complete set of AGK-based cut enhanced graphs has been derived in [12], the corresponding contributions being expressed via the ones of cut net-fan sub-graphs. The principal observation made in [12] was that all cut enhanced diagrams can be divided in two classes. The diagrams of the first kind are characterized by a “tree”-like structure of *cut Pomerons*; they consist of cut and uncut net-fans coupled together in some “central” (not necessarily unique) vertex, such that each of the cut net-fan sub-graphs is characterized by a fan-like structure of cut Pomerons. All other graphs belong to the second class; they contain sequences of *cut Pomerons* arranged in a “zigzag” way, with subsequent Pomeron end rapidities satisfying  $y_1 > y_2 < y_3 > \dots$ ; they are expressed via zigzag-like cuts of net-fan sub-graphs.<sup>11</sup> Most importantly, such diagrams give zero contribution to the total cross section and negligible corrections for diffractive ones. Thus, in our analysis we can safely restrict ourselves with the tree-like cut graphs only. In the following, we shall start with the full set of the corresponding diagrams, derived in [12], selecting from them the ones which lead to the desirable diffractive topologies of final states. For certain graphs, this will require to replace the general cut net-fan contributions (with the fan-like structure of cut Pomerons) by the ones corresponding to a rapidity gap between a given (say, projectile) proton and the nearest cut multi-Pomeron vertex.

The complete set of AGK-based cuts of net-fan diagrams, characterized by the fan-like structure of cuts, is generated by the Schwinger-Dyson equations of Fig. 20 [12]. The top line of the Figure

<sup>11</sup>More detailed discussion and examples of diagrams of both kinds can be found in [11, 12].



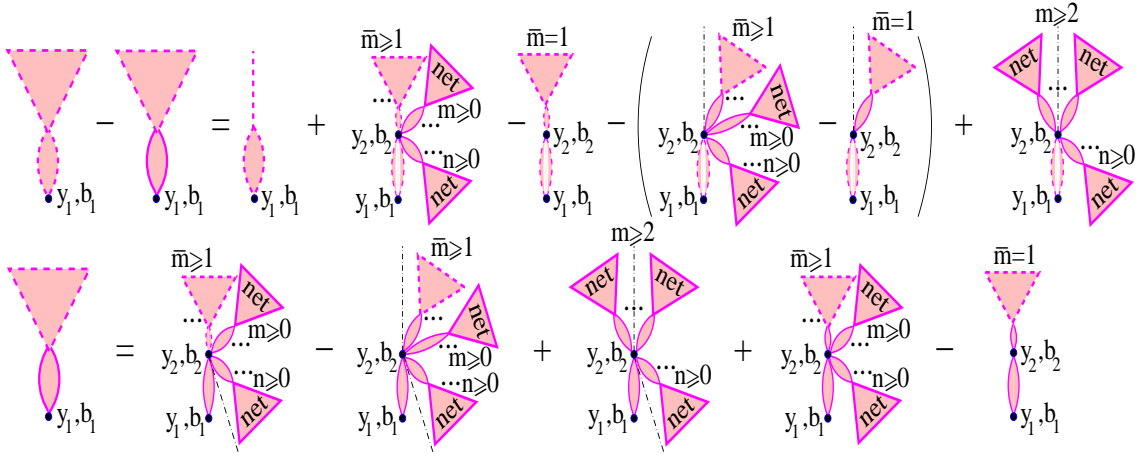


Figure 20: Recursive representations for cut net-fan diagrams characterized by a fan-like structure of cuts. The top line of the Figure defines the contribution  $2\hat{\chi}_{jk}^{\text{fan}}$  of the subset of graphs, in which the handle of the fan is cut (the symbolic drawing for the cut handle is explained in Fig. 21), whereas the bottom line gives the one of the diagrams, where the cut plane (indicated by dot-dashed lines) goes aside the vertex  $(y_1, b_1)$ ,  $2\tilde{\chi}_{jk}^{\text{fan}}$ .

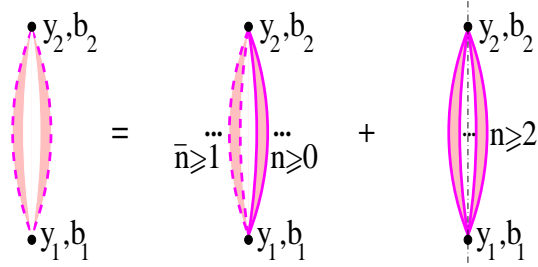


Figure 21: Cutting a general 2-point sequence of Pomeron and Pomeron loops, exchanged between two cells of the Pomeron net (vertices  $(y_1, b_1)$  and  $(y_2, b_2)$  in the picture), one obtains two kinds of contributions: i) with  $\bar{n} \geq 1$  cut and  $n \geq 0$  uncut irreducible 2-point loop sequences (1st graph in the r.h.s.); ii) with the cut plane passing between  $n \geq 2$  uncut irreducible 2-point loop sequences (2nd graph in the r.h.s.).

defines the contribution  $2\hat{\chi}_{jk}^{\text{fan}}$  of the subset, in which the handle of the fan is cut, i.e. with the cut plane passing through the original vertex  $(y_1, b_1)$ . In such a case, one or a number of irreducible 2-point sequences of Pomeron and Pomeron loops, connected to the vertex  $(y_1, b_1)$ , is cut, as depicted in the 1st graph in the r.h.s. of Fig. 21, or, alternatively, the cut plane passes between those sequences as in the 2nd graph in the r.h.s. of Fig. 21. In turn, the bottom line of Fig. 20 gives the contribution  $2\tilde{\chi}_{jk}^{\text{fan}}$  of other fan-like cuts of net-fans, where the handle of the fan is uncut, i.e. when the cut plane passes aside the vertex  $(y_1, b_1)$ .

Concerning the diagrams in the top line of Fig. 20, the first graph in the r.h.s. corresponds to all possible AGK-based cuts of the single 2-point sequence of Pomeron and Pomeron loops exchanged between the vertex  $(y_1, b_1)$  and the projectile proton (the 1st graph in the r.h.s. of Fig. 4). The 2nd diagram describes the development of the cut Pomeron net, with the vertex  $(y_2, b_2)$  coupling together  $\bar{m} \geq 1$  cut projectile net-fans, each one characterized by the fan-like structure of cuts, and any numbers  $m, n \geq 0$  of uncut projectile and target net-fans. There one has to subtract the contribution of the 3rd graph corresponding to the Pomeron self-coupling ( $\bar{m} = 1; m, n = 0$ ) and

the ones of the next two diagrams which correspond to a configuration of non-AGK type, where in all the  $\bar{m}$  cut net-fans connected to the vertex  $(y_2, b_2)$  the handles of the fans remain uncut and are situated on the same side of the cut plane, together with all the  $m$  uncut projectile net-fans. Finally, in the last graph in the top line of the Figure the cut plane passes between  $m \geq 2$  uncut projectile net-fans with at least one of them remained on either side of the cut, such that a rapidity gap is formed between the projectile proton and the vertex  $(y_2, b_2)$ .

The first three diagrams in the r.h.s. of the bottom line of Fig. 20 are similar to their corresponding counterparts in the top line, with the difference that the handle of the fan is now uncut. Therefore, there are  $n \geq 1$  uncut target net-fans connected to the vertex  $(y_2, b_2)$ , such that at least one of them is positioned on the opposite side of the cut plane with respect to the vertex  $(y_1, b_1)$ . In turn, the 4th graph describes the situation when the cut plane goes aside the vertex  $(y_2, b_2)$ . In such a case, there are  $\bar{m} \geq 1$  projectile net-fans coupled to that vertex, which are cut in a fan-like way and have their handles uncut and positioned on the same side of the cut plane, together with any numbers  $m \geq 0$  of projectile and  $n \geq 0$  of target uncut net-fans. There one has to subtract the Pomeron self-coupling ( $\bar{m} = 1; m, n = 0$ ) described by the last diagram in the line.

As demonstrated in [12], the total contribution  $2\bar{\chi}_{jk}^{\text{fan}} \equiv 2\hat{\chi}_{jk}^{\text{fan}} + 2\tilde{\chi}_{jk}^{\text{fan}}$  of fan-like cuts of net-fans coincides with twice the uncut one:

$$2\bar{\chi}_{jk}^{\text{fan}}(y_1, \vec{b}_1|Y, \vec{b}) = 2\chi_{jk}^{\text{net}}(y_1, \vec{b}_1|Y, \vec{b}), \quad (43)$$

whereas for the one of the subset with a cut handle one obtains the recursive equation

$$\begin{aligned} 2\hat{\chi}_{jk}^{\text{fan}}(y_1, \vec{b}_1|Y, \vec{b}) &= 2\chi_j^{\text{loop}}(y_1, b_1) + 2G \int_{\xi}^{y_1-\xi} dy_2 \int d^2b_2 \left( 1 - e^{-\chi^{\text{loop}}(y_1-y_2, |\vec{b}_1-\vec{b}_2|)} \right) \\ &\times \left[ \left( 1 - e^{-\hat{\chi}_{jk}^{\text{fan}}(y_2, \vec{b}_2|Y, \vec{b})} \right) e^{-2\chi_{kj}^{\text{net}}(Y-y_2, \vec{b}-\vec{b}_2|Y, \vec{b})} - \hat{\chi}_{jk}^{\text{fan}}(y_2, \vec{b}_2|Y, \vec{b}) \right]. \end{aligned} \quad (44)$$

However, in the following we shall need to choose elastic, respectively inelastic, intermediate hadronic states for diffractive topologies, as discussed in Section 3. Thus, we have to obtain the contribution of fan-like cuts of net-fans  $2\bar{\chi}_{jk_1k_2}^{\text{fan}}$  of Fig. 20, considering different elastic scattering eigenstates  $|k_1\rangle$  and  $|k_2\rangle$  to the left and to the right of the cut plane for the partner (here, target) proton. In addition, considering the graphs with an uncut handle (bottom line of Fig. 20), we have to distinguish the contributions when the vertex  $(y_1, b_1)$  is positioned to the left ( $\tilde{\chi}_{jk_1k_2}^{\text{fan}(l)}$ ) and to the right ( $\tilde{\chi}_{jk_1k_2}^{\text{fan}(r)}$ ) of the cut. Proceeding as in Ref. [12], we obtain instead of (43-44)

$$2\bar{\chi}_{jk_1k_2}^{\text{fan}}(y_1, \vec{b}_1|Y, \vec{b}) = \chi_{jk_1}^{\text{net}}(y_1, \vec{b}_1|Y, \vec{b}) + \chi_{jk_2}^{\text{net}}(y_1, \vec{b}_1|Y, \vec{b}). \quad (45)$$

$$\begin{aligned} 2\hat{\chi}_{jk_1k_2}^{\text{fan}}(y_1, \vec{b}_1|Y, \vec{b}) &= 2\chi_j^{\text{loop}}(y_1, b_1) + 2G \int_{\xi}^{y_1-\xi} dy_2 \int d^2b_2 \left( 1 - e^{-\chi^{\text{loop}}(y_1-y_2, |\vec{b}_1-\vec{b}_2|)} \right) \\ &\times \left[ \left( 1 - e^{-\hat{\chi}_{jk_1k_2}^{\text{fan}}(y_2, \vec{b}_2|Y, \vec{b})} \right) e^{-\chi_{k_1j}^{\text{net}}(Y-y_2, \vec{b}-\vec{b}_2|Y, \vec{b}) - \chi_{k_2j}^{\text{net}}(Y-y_2, \vec{b}-\vec{b}_2|Y, \vec{b})} - \hat{\chi}_{jk_1k_2}^{\text{fan}}(y_2, \vec{b}_2|Y, \vec{b}) \right] \end{aligned} \quad (46)$$

$$\tilde{\chi}_{jk_1k_2}^{\text{fan}(l)}(y_1, \vec{b}_1|Y, \vec{b}) = \chi_{jk_1}^{\text{net}}(y_1, \vec{b}_1|Y, \vec{b}) - \hat{\chi}_{jk_1k_2}^{\text{fan}}(y_1, \vec{b}_1|Y, \vec{b}) \quad (47)$$

$$\tilde{\chi}_{jk_1k_2}^{\text{fan}(r)}(y_1, \vec{b}_1|Y, \vec{b}) = \chi_{jk_2}^{\text{net}}(y_1, \vec{b}_1|Y, \vec{b}) - \hat{\chi}_{jk_1k_2}^{\text{fan}}(y_1, \vec{b}_1|Y, \vec{b}). \quad (48)$$

Let us now derive contributions of diffractive cuts of net-fans, which correspond to having a rapidity gap between the projectile proton<sup>12</sup> and all the secondary particles produced. The corresponding recursive representations shown in Fig. 22 are easily obtained from the ones of Fig. 20 by merely replacing the contributions of general fan-like cuts of net-fan graphs by the diffractive ones (shown as open ‘‘forks’’), each corresponding to a rapidity gap of size  $y_{\text{gap}}$  or larger. Considering now generally different elastic scattering eigenstates both for the projectile and the

<sup>12</sup>For definiteness, we speak here about diffractive cuts of the projectile net-fan.

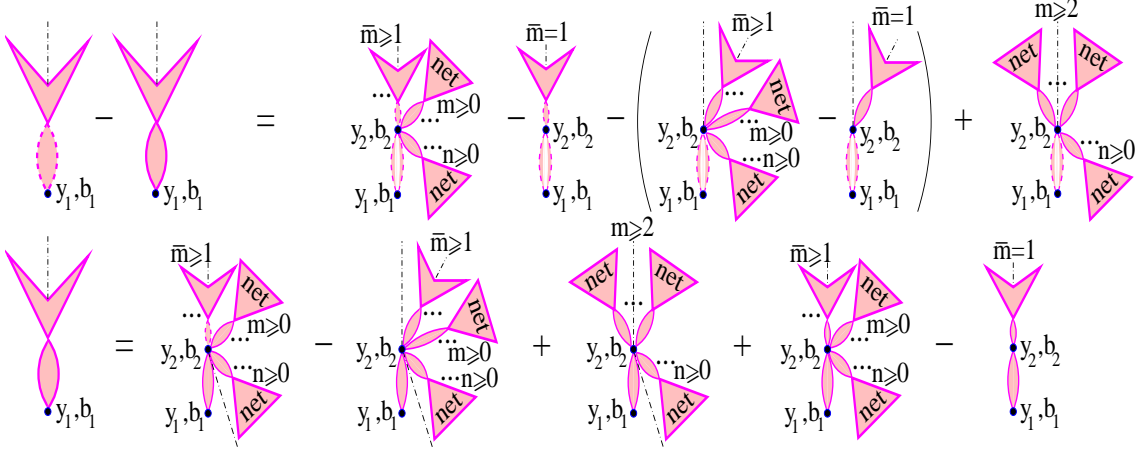


Figure 22: Recursive representations for diffractive cuts of net-fan diagrams: the contribution  $2\bar{\chi}_{j_1 j_2 k_1 k_2}^D - \bar{\chi}_{j_1 j_2 k_1 k_2}^{D(l)} - \bar{\chi}_{j_1 j_2 k_1 k_2}^{D(r)}$  of the graphs with the handle of the fan being cut (top line) and the one with the uncut handle  $\bar{\chi}_{j_1 j_2 k_1 k_2}^{D(l)} + \bar{\chi}_{j_1 j_2 k_1 k_2}^{D(r)}$  (bottom line).

target protons, we get

$$\begin{aligned}
2\bar{\chi}_{j_1 j_2 k_1 k_2}^D(y_1, \vec{b}_1, y_{\text{gap}}|Y, \vec{b}) &= \frac{G}{2} \int_{\max(y_{\text{gap}}, \xi)}^{y_1 - \xi} dy_2 \int d^2 b_2 \left[ 1 - e^{-\chi^{\text{loop}}(y_1 - y_2, |\vec{b}_1 - \vec{b}_2|)} \right] \\
&\times \left\{ \left( e^{-\chi_{k_1 j_1}^{\text{net}}(Y - y_2, \vec{b} - \vec{b}_2|Y, \vec{b})} + e^{-\chi_{k_2 j_2}^{\text{net}}(Y - y_2, \vec{b} - \vec{b}_2|Y, \vec{b})} \right) \left[ \left( 1 - e^{-\chi_{j_1 k_1}^{\text{net}}(y_2, \vec{b}_2|Y, \vec{b})} \right) \right. \right. \\
&\times \left. \left( 1 - e^{-\chi_{j_2 k_2}^{\text{net}}(y_2, \vec{b}_2|Y, \vec{b})} \right) + \left( e^{2\bar{\chi}_{j_1 j_2 k_1 k_2}^D(y_2, \vec{b}_2, y_{\text{gap}}|Y, \vec{b})} - 1 \right) e^{-\chi_{j_1 k_1}^{\text{net}}(y_2, \vec{b}_2|Y, \vec{b}) - \chi_{j_2 k_2}^{\text{net}}(y_2, \vec{b}_2|Y, \vec{b})} \right] \\
&- 4\bar{\chi}_{j_1 j_2 k_1 k_2}^D(y_2, \vec{b}_2, y_{\text{gap}}|Y, \vec{b}) + \left( e^{-\chi_{k_1 j_1}^{\text{net}}(Y - y_2, \vec{b} - \vec{b}_2|Y, \vec{b})} - e^{-\chi_{k_2 j_2}^{\text{net}}(Y - y_2, \vec{b} - \vec{b}_2|Y, \vec{b})} \right) \\
&\times \left. \left[ \left( e^{\bar{\chi}_{j_1 j_2 k_1 k_2}^{D(l)}(y_2, \vec{b}_2, y_{\text{gap}}|Y, \vec{b})} - 1 \right) e^{-\chi_{j_1 k_1}^{\text{net}}(y_2, \vec{b}_2|Y, \vec{b})} - \left( e^{\bar{\chi}_{j_1 j_2 k_1 k_2}^{D(r)}(y_2, \vec{b}_2, y_{\text{gap}}|Y, \vec{b})} - 1 \right) e^{-\chi_{j_2 k_2}^{\text{net}}(y_2, \vec{b}_2|Y, \vec{b})} \right] \right\} \quad (49)
\end{aligned}$$

$$\begin{aligned}
\bar{\chi}_{j_1 j_2 k_1 k_2}^{D(l)}(y_1, \vec{b}_1, y_{\text{gap}}|Y, \vec{b}) &= \frac{G}{2} \int_{\max(y_{\text{gap}}, \xi)}^{y_1 - \xi} dy_2 \int d^2 b_2 \left[ 1 - e^{-\chi^{\text{loop}}(y_1 - y_2, |\vec{b}_1 - \vec{b}_2|)} \right] \\
&\times \left\{ e^{-\chi_{k_1 j_1}^{\text{net}}(Y - y_2, \vec{b} - \vec{b}_2|Y, \vec{b})} \left( 1 - e^{-\chi_{k_2 j_2}^{\text{net}}(Y - y_2, \vec{b} - \vec{b}_2|Y, \vec{b})} \right) \left[ \left( 1 - e^{-\chi_{j_1 k_1}^{\text{net}}(y_2, \vec{b}_2|Y, \vec{b})} \right) \right. \right. \\
&\times \left. \left( 1 - e^{-\chi_{j_2 k_2}^{\text{net}}(y_2, \vec{b}_2|Y, \vec{b})} \right) + \left( e^{2\bar{\chi}_{j_1 j_2 k_1 k_2}^D(y_2, \vec{b}_2, y_{\text{gap}}|Y, \vec{b})} - 1 \right) e^{-\chi_{j_1 k_1}^{\text{net}}(y_2, \vec{b}_2|Y, \vec{b}) - \chi_{j_2 k_2}^{\text{net}}(y_2, \vec{b}_2|Y, \vec{b})} \right. \\
&- \left. \left. \left( e^{\bar{\chi}_{j_1 j_2 k_1 k_2}^{D(r)}(y_2, \vec{b}_2, y_{\text{gap}}|Y, \vec{b})} - 1 \right) e^{-\chi_{j_2 k_2}^{\text{net}}(y_2, \vec{b}_2|Y, \vec{b})} \right] + \left( e^{\bar{\chi}_{j_1 j_2 k_1 k_2}^{D(l)}(y_2, \vec{b}_2, y_{\text{gap}}|Y, \vec{b})} - 1 \right) \right. \\
&\times \left. \left. e^{-\chi_{j_1 k_1}^{\text{net}}(y_2, \vec{b}_2|Y, \vec{b}) - \chi_{k_1 j_1}^{\text{net}}(Y - y_2, \vec{b} - \vec{b}_2|Y, \vec{b})} \left( 1 + e^{-\chi_{k_2 j_2}^{\text{net}}(Y - y_2, \vec{b} - \vec{b}_2|Y, \vec{b})} \right) - 2\bar{\chi}_{j_1 j_2 k_1 k_2}^{D(l)}(y_2, \vec{b}_2, y_{\text{gap}}|Y, \vec{b}) \right\} \quad (50)
\end{aligned}$$

$$\bar{\chi}_{j_1 j_2 k_1 k_2}^{D(r)}(y_1, \vec{b}_1, y_{\text{gap}}|Y, \vec{b}) = \bar{\chi}_{j_2 j_1 k_2 k_1}^{D(l)}(y_1, \vec{b}_1, y_{\text{gap}}|Y, \vec{b}), \quad (51)$$

where  $2\bar{\chi}_{j_1 j_2 k_1 k_2}^D$  is the total contribution of diffractively cut net-fan graphs, whereas  $\bar{\chi}_{j_1 j_2 k_1 k_2}^{D(l)}$  and  $\bar{\chi}_{j_1 j_2 k_1 k_2}^{D(r)}$  are the ones with the handle of the fan being uncut and positioned respectively to the left and to the right from the cut plane.

Now, starting from the full set of irreducible tree-like cut enhanced diagrams derived in [12] (Figs. 15-17, 19 of the paper), we can obtain the complete subsets of cut enhanced graphs, which produce rapidity gaps in the forward or/and in the backward direction by merely replacing the contributions of fan-like cuts of net-fans  $2\bar{\chi}^{\text{fan}}$ ,  $\bar{\chi}^{\text{fan}}$  in the corresponding diagrams by the ones of diffractive cuts  $2\bar{\chi}^D$ ,  $\bar{\chi}^{D(l/r)}$ , like we did when deriving the representation of Fig. 22 for the

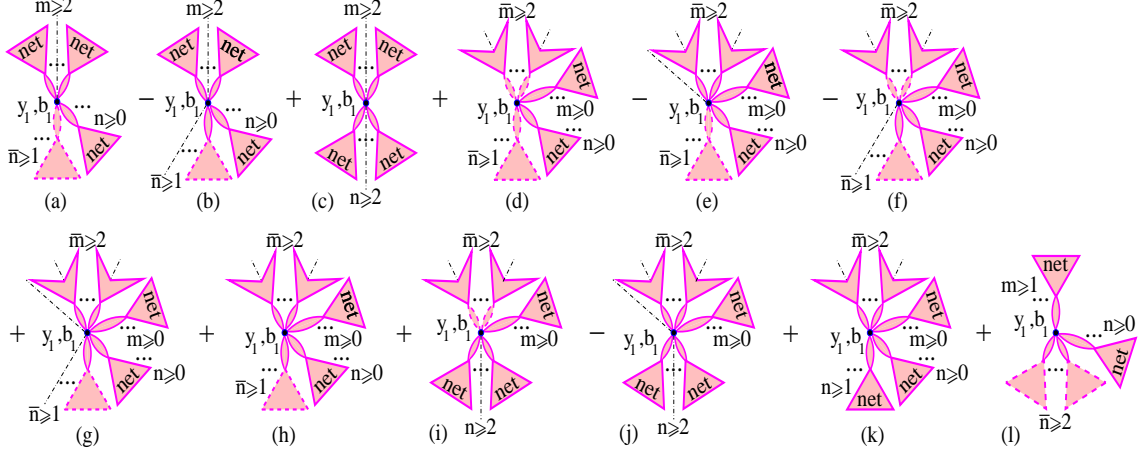


Figure 23: Complete set of irreducible cut diagrams which produce a LRG between the quasi-elastically scattered projectile proton and all the secondary particles produced.

latter. This way, for the sum of the two contributions  $2\chi_{j_1 j_2 k}^{1-\text{gap}}(Y, b, y_{\text{gap}}) + 2\chi_{j_1 j_2 k k}^{2-\text{gap}}(Y, b, y_{\text{gap}}, \xi)$  corresponding to a LRG of size  $y_{\text{gap}}$  or larger between the quasi-elastically scattered projectile proton and all other particles produced (and, possibly, an additional one in the backward direction) we obtain the set of graphs of Fig. 23.

The diagram in Fig. 23 (a) has explicitly the *ABC*-like diffractive structure of Fig. 8 (a), with the blocks *A* and *B* being represented by any numbers ( $\geq 1$ ) of uncut projectile net-fans and the block *C* containing  $\bar{n} \geq 1$  cut and  $n \geq 0$  uncut target net-fans. Here we have to subtract the non-AGK type configurations of the graph in Fig. 23 (b), which corresponds to the situation when all the  $\bar{n}$  cut target net-fans have their handles uncut and positioned on the same side of the cut, together with all the  $n$  uncut target net-fans. The set of diagrams generated by the graphs of Fig. 23 (a,b) contains all the lowest order ones of Fig. 9 and of Fig. 10 (f-h), dominating the diffractive contribution  $2\chi^{1-\text{gap}}$ . Applying the Reggeon diagram technique and taking into account (45-48), we obtain for them

$$G \int_{\xi}^{\min(Y-\xi, Y-y_{\text{gap}})} dy_1 \int d^2 b_1 \left( 1 - e^{-\chi_{j_1 k}^{\text{net}}(Y-y_1, \vec{b}-\vec{b}_1 | Y, \vec{b})} \right) \left( 1 - e^{-\chi_{j_2 k}^{\text{net}}(Y-y_1, \vec{b}-\vec{b}_1 | Y, \vec{b})} \right) \times \left[ 1 - e^{-\chi_{k j_1 j_2}^{\text{fan}}(y_1, \vec{b}_1 | Y, \vec{b})} - \frac{1}{2} \left( 1 - e^{-\chi_{k j_1}^{\text{net}}(y_1, \vec{b}_1 | Y, \vec{b})} \right) \left( 1 - e^{-\chi_{k j_2}^{\text{net}}(y_1, \vec{b}_1 | Y, \vec{b})} \right) \right]. \quad (52)$$

In turn, the set of diagrams generated by the graph in Fig. 23 (c) contains the ones of Fig. 10 (a-e) and describes the production of a low mass diffractive state at central rapidities, with the contribution

$$\frac{G}{2} \int_{\xi}^{\min(Y-\xi, Y-y_{\text{gap}})} dy_1 \int d^2 b_1 \left( 1 - e^{-\chi_{j_1 k}^{\text{net}}(Y-y_1, \vec{b}-\vec{b}_1 | Y, \vec{b})} \right) \left( 1 - e^{-\chi_{j_2 k}^{\text{net}}(Y-y_1, \vec{b}-\vec{b}_1 | Y, \vec{b})} \right) \times \left( 1 - e^{-\chi_{k j_1}^{\text{net}}(y_1, \vec{b}_1 | Y, \vec{b})} \right) \left( 1 - e^{-\chi_{k j_2}^{\text{net}}(y_1, \vec{b}_1 | Y, \vec{b})} \right). \quad (53)$$

All the other graphs in Fig. 23 are much less important, the corresponding contributions being proportional to the third or higher power of the triple-Pomeron coupling. Indeed, the diagrams in Fig. 23 (d-k) contain  $\bar{m} \geq 2$  diffractively cut projectile net-fans whereas the one in Fig. 23 (l) contains  $\bar{n} \geq 2$  cut target net-fans with uncut handles; each of these sub-graphs contains at least one internal multi-Pomeron vertex. By consequence, the graphs of Fig. 23 (d-l) are sub-dominant at large impact parameters whereas at small ones they are suppressed by exponential factors (see

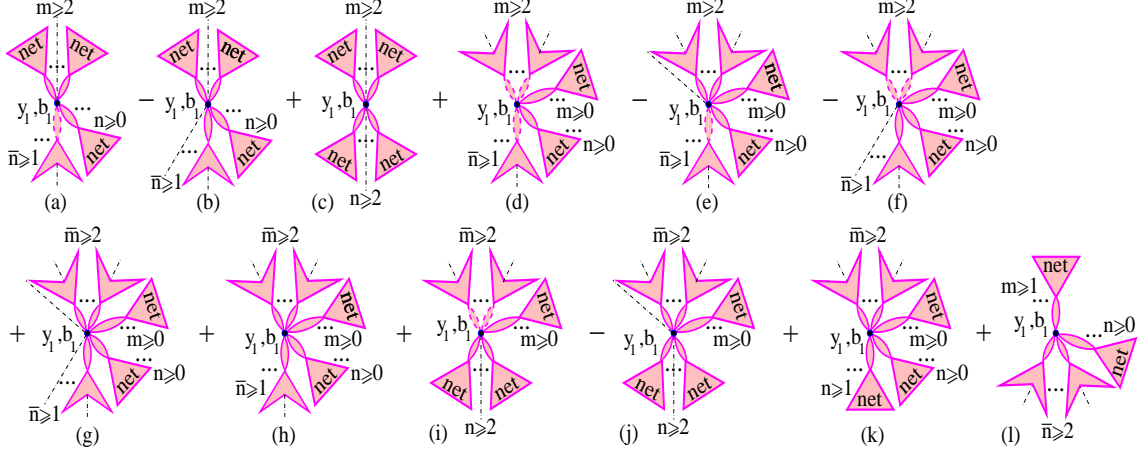


Figure 24: Complete set of irreducible cut diagrams corresponding to central diffraction topology of the final state.

the discussion in Section 3.2). Calculating their contributions and adding them to (52-53), we obtain

$$\begin{aligned}
& 2\chi_{j_1 j_2 k}^{1-\text{gap}}(Y, b, y_{\text{gap}}) + 2\chi_{j_1 j_2 k k}^{2-\text{gap}}(Y, b, y_{\text{gap}}, \xi) = G \int_{\xi}^{\min(Y-\xi, Y-y_{\text{gap}})} dy_1 \int d^2 b_1 \\
& \times \left\{ \left[ \left( 1 - e^{-\chi_{j_1 k}^{\text{net}}(Y-y_1, \vec{b}-\vec{b}_1|Y, \vec{b})} \right) \left( 1 - e^{-\chi_{j_2 k}^{\text{net}}(Y-y_1, \vec{b}-\vec{b}_1|Y, \vec{b})} \right) + \left( e^{2\tilde{\chi}_{j_1 j_2 k k}^{\text{D}}(Y-y_1, \vec{b}-\vec{b}_1, y_{\text{gap}}|Y, \vec{b})} \right. \right. \\
& \quad \left. \left. - 1 - 2\tilde{\chi}_{j_1 j_2 k k}^{\text{D}}(Y-y_1, \vec{b}-\vec{b}_1, y_{\text{gap}}|Y, \vec{b}) \right) e^{-\chi_{j_1 k}^{\text{net}}(Y-y_1, \vec{b}-\vec{b}_1|Y, \vec{b}) - \chi_{j_2 k}^{\text{net}}(Y-y_1, \vec{b}-\vec{b}_1|Y, \vec{b})} \right] \\
& \quad \times \left( 1 - e^{-\tilde{\chi}_{k j_1 j_2}^{\text{fan}}(y_1, \vec{b}_1|Y, \vec{b})} \right) - \frac{1}{2} \left( e^{-\chi_{k j_1}^{\text{net}}(y_1, \vec{b}_1|Y, \vec{b})} - e^{-\chi_{k j_2}^{\text{net}}(y_1, \vec{b}_1|Y, \vec{b})} \right) \\
& \times \left[ \left( e^{\tilde{\chi}_{j_1 j_2 k k}^{\text{D}(l)}(Y-y_1, \vec{b}-\vec{b}_1, y_{\text{gap}}|Y, \vec{b})} - 1 - \tilde{\chi}_{j_1 j_2 k k}^{\text{D}(l)}(Y-y_1, \vec{b}-\vec{b}_1, y_{\text{gap}}|Y, \vec{b}) \right) e^{-\chi_{j_1 k}^{\text{net}}(Y-y_1, \vec{b}-\vec{b}_1|Y, \vec{b})} \right. \\
& \quad \left. - \left( e^{\tilde{\chi}_{j_1 j_2 k k}^{\text{D}(r)}(Y-y_1, \vec{b}-\vec{b}_1, y_{\text{gap}}|Y, \vec{b})} - 1 - \tilde{\chi}_{j_1 j_2 k k}^{\text{D}(r)}(Y-y_1, \vec{b}-\vec{b}_1, y_{\text{gap}}|Y, \vec{b}) \right) e^{-\chi_{j_2 k}^{\text{net}}(Y-y_1, \vec{b}-\vec{b}_1|Y, \vec{b})} \right] \\
& \quad + \left( 1 - e^{-\chi_{j_1 k}^{\text{net}}(Y-y_1, \vec{b}-\vec{b}_1|Y, \vec{b})} \right) \left( e^{\tilde{\chi}_{k j_1 j_2}^{\text{fan}(l)}(y_1, \vec{b}_1|Y, \vec{b})} - 1 - \tilde{\chi}_{k j_1 j_2}^{\text{fan}(l)}(y_1, \vec{b}_1|Y, \vec{b}) \right) e^{-\chi_{k j_1}^{\text{net}}(y_1, \vec{b}_1|Y, \vec{b})} \\
& \quad + \left( 1 - e^{-\chi_{j_2 k}^{\text{net}}(Y-y_1, \vec{b}-\vec{b}_1|Y, \vec{b})} \right) \left( e^{\tilde{\chi}_{k j_1 j_2}^{\text{fan}(r)}(y_1, \vec{b}_1|Y, \vec{b})} - 1 - \tilde{\chi}_{k j_1 j_2}^{\text{fan}(r)}(y_1, \vec{b}_1|Y, \vec{b}) \right) e^{-\chi_{k j_2}^{\text{net}}(y_1, \vec{b}_1|Y, \vec{b})} \left. \right\} \quad (54)
\end{aligned}$$

Replacing now in Fig. 23 the contributions of fan-like cuts of target net-fans  $2\tilde{\chi}^{\text{fan}}$ ,  $\tilde{\chi}^{\text{fan}(l/r)}$  by the ones of the diffractive cuts  $2\tilde{\chi}^{\text{D}}$ ,  $\tilde{\chi}^{\text{D}(l/r)}$ , we obtain the complete set of irreducible cut diagrams for central diffraction, as depicted in Fig. 24, with the contribution

$$\begin{aligned}
& 2\chi_{j_1 j_2 k_1 k_2}^{2-\text{gap}}(Y, b, y_{\text{gap}}^{(f)}, y_{\text{gap}}^{(b)}) = \frac{G}{2} \int_{\max(\xi, y_{\text{gap}}^{(b)})}^{\min(Y-\xi, Y-y_{\text{gap}}^{(f)})} dy_1 \int d^2 b_1 \\
& \times \left\{ \left[ \left( 1 - e^{-\chi_{j_1 k_1}^{\text{net}}(Y-y_1, \vec{b}-\vec{b}_1|Y, \vec{b})} \right) \left( 1 - e^{-\chi_{j_2 k_2}^{\text{net}}(Y-y_1, \vec{b}-\vec{b}_1|Y, \vec{b})} \right) + \left( e^{2\tilde{\chi}_{j_1 j_2 k_1 k_2}^{\text{D}}(Y-y_1, \vec{b}-\vec{b}_1, y_{\text{gap}}^{(f)}|Y, \vec{b})} \right. \right. \\
& \quad \left. \left. - 1 - 2\tilde{\chi}_{j_1 j_2 k_1 k_2}^{\text{D}}(Y-y_1, \vec{b}-\vec{b}_1, y_{\text{gap}}^{(f)}|Y, \vec{b}) \right) e^{-\chi_{j_1 k_1}^{\text{net}}(Y-y_1, \vec{b}-\vec{b}_1|Y, \vec{b}) - \chi_{j_2 k_2}^{\text{net}}(Y-y_1, \vec{b}-\vec{b}_1|Y, \vec{b})} \right] \\
& \quad \times \left[ 1 - e^{\tilde{\chi}_{k_1 k_2 j_1 j_2}^{\text{D}(l)}(y_1, \vec{b}_1, y_{\text{gap}}^{(b)}|Y, \vec{b}) - \chi_{k_1 j_1}^{\text{net}}(y_1, \vec{b}_1|Y, \vec{b})} - e^{\tilde{\chi}_{k_1 k_2 j_1 j_2}^{\text{D}(r)}(y_1, \vec{b}_1, y_{\text{gap}}^{(b)}|Y, \vec{b}) - \chi_{k_2 j_2}^{\text{net}}(y_1, \vec{b}_1|Y, \vec{b})} \right. \\
& \quad \quad \left. + e^{2\tilde{\chi}_{k_1 k_2 j_1 j_2}^{\text{D}}(y_1, \vec{b}_1, y_{\text{gap}}^{(b)}|Y, \vec{b}) - \chi_{k_1 j_1}^{\text{net}}(y_1, \vec{b}_1|Y, \vec{b}) - \chi_{k_2 j_2}^{\text{net}}(y_1, \vec{b}_1|Y, \vec{b})} \right] \\
& \quad + \left( e^{\tilde{\chi}_{j_1 j_2 k_1 k_2}^{\text{D}(l)}(Y-y_1, \vec{b}-\vec{b}_1, y_{\text{gap}}^{(f)}|Y, \vec{b})} - 1 - \tilde{\chi}_{j_1 j_2 k_1 k_2}^{\text{D}(l)}(Y-y_1, \vec{b}-\vec{b}_1, y_{\text{gap}}^{(f)}|Y, \vec{b}) \right) e^{-\chi_{j_1 k_1}^{\text{net}}(Y-y_1, \vec{b}-\vec{b}_1|Y, \vec{b})}
\end{aligned}$$

$$\begin{aligned}
& \times \left[ 1 - e^{-\chi_{k_1 j_1}^{\text{net}}(y_1, \vec{b}_1 | Y, \vec{b})} + e^{-\chi_{k_2 j_2}^{\text{net}}(y_1, \vec{b}_1 | Y, \vec{b})} - e^{2\tilde{\chi}_{k_1 k_2 j_1 j_2}^{\text{D}}(y_1, \vec{b}_1, y_{\text{gap}}^{(\text{b})} | Y, \vec{b})} - \chi_{k_1 j_1}^{\text{net}}(y_1, \vec{b}_1 | Y, \vec{b}) - \chi_{k_2 j_2}^{\text{net}}(y_1, \vec{b}_1 | Y, \vec{b}) \right] \\
& \quad + \left( e^{\tilde{\chi}_{j_1 j_2 k_1 k_2}^{\text{D}(\text{r})}(Y - y_1, \vec{b} - \vec{b}_1, y_{\text{gap}} | Y, \vec{b})} - 1 - \tilde{\chi}_{j_1 j_2 k_1 k_2}^{\text{D}(\text{r})}(Y - y_1, \vec{b} - \vec{b}_1, y_{\text{gap}} | Y, \vec{b}) \right) e^{-\chi_{j_2 k_2}^{\text{net}}(Y - y_1, \vec{b} - \vec{b}_1 | Y, \vec{b})} \\
& \times \left[ 1 + e^{-\chi_{k_1 j_1}^{\text{net}}(y_1, \vec{b}_1 | Y, \vec{b})} - e^{-\chi_{k_2 j_2}^{\text{net}}(y_1, \vec{b}_1 | Y, \vec{b})} - e^{2\tilde{\chi}_{k_1 k_2 j_1 j_2}^{\text{D}}(y_1, \vec{b}_1, y_{\text{gap}}^{(\text{b})} | Y, \vec{b})} - \chi_{k_1 j_1}^{\text{net}}(y_1, \vec{b}_1 | Y, \vec{b}) - \chi_{k_2 j_2}^{\text{net}}(y_1, \vec{b}_1 | Y, \vec{b}) \right] \\
& \quad + 2 \left( 1 - e^{-\chi_{j_1 k_1}^{\text{net}}(Y - y_1, \vec{b} - \vec{b}_1 | Y, \vec{b})} \right) \left( e^{\tilde{\chi}_{k_1 k_2 j_1 j_2}^{\text{D}(\text{l})}(y_1, \vec{b}_1, y_{\text{gap}}^{(\text{b})} | Y, \vec{b})} - 1 - \tilde{\chi}_{k_1 k_2 j_1 j_2}^{\text{D}(\text{l})}(y_1, \vec{b}_1, y_{\text{gap}}^{(\text{b})} | Y, \vec{b}) \right) \\
& \quad \quad \quad \times e^{-\chi_{k_1 j_1}^{\text{net}}(y_1, \vec{b}_1 | Y, \vec{b})} + 2 \left( 1 - e^{-\chi_{j_2 k_2}^{\text{net}}(Y - y_1, \vec{b} - \vec{b}_1 | Y, \vec{b})} \right) \\
& \quad \quad \quad \times \left( e^{\tilde{\chi}_{k_1 k_2 j_1 j_2}^{\text{D}(\text{r})}(y_1, \vec{b}_1, y_{\text{gap}}^{(\text{b})} | Y, \vec{b})} - 1 - \tilde{\chi}_{k_1 k_2 j_1 j_2}^{\text{D}(\text{r})}(y_1, \vec{b}_1, y_{\text{gap}}^{(\text{b})} | Y, \vec{b}) \right) e^{-\chi_{k_2 j_2}^{\text{net}}(y_1, \vec{b}_1 | Y, \vec{b})} \}. \quad (55)
\end{aligned}$$

In a similar way one can obtain the set of irreducible cut graphs which produce a central rapidity gap. For brevity, we give here the corresponding contribution without derivation:

$$\begin{aligned}
2\chi_{jk}^{\text{c-gap}}(Y, b, y_{\text{gap}}) &= \frac{G^2}{4} \int_{\max(\xi + y_{\text{gap}}, 2\xi)}^{Y - \xi} dy_1 \int_{\xi}^{y_1 - \max(y_{\text{gap}}, \xi)} dy_2 \int d^2 b_1 d^2 b_2 \\
& \times \left\{ \left( 1 - e^{-\chi^{\text{loop}}(y_1 - y_2, |\vec{b}_1 - \vec{b}_2|)} \right)^2 \left[ 1 - e^{2\tilde{\chi}_{jjkk}^{\text{D}}(1) - 2\chi_{jk}^{\text{net}}(1)} - 2 \left( e^{-\hat{\chi}_{jjkk}^{\text{fan}}(1)} - e^{\tilde{\chi}_{jjkk}^{\text{D}(\text{l})}(1) - \chi_{jk}^{\text{net}}(1)} \right) \right] \right. \\
& \quad \times \left[ 1 - e^{2\tilde{\chi}_{kkjj}^{\text{D}}(2) - 2\chi_{kj}^{\text{net}}(2)} - 2 \left( e^{-\hat{\chi}_{kkjj}^{\text{fan}}(2)} - e^{\tilde{\chi}_{kkjj}^{\text{D}(\text{l})}(2) - \chi_{kj}^{\text{net}}(2)} \right) \right] e^{-2\chi_{kj}^{\text{net}}(2) - 2\chi_{kj}^{\text{net}}(1)} \\
& \quad - 2 \left( 1 - e^{-\chi^{\text{loop}}(y_1 - y_2, |\vec{b}_1 - \vec{b}_2|)} \right) \left[ \left( 1 - e^{2\tilde{\chi}_{jjkk}^{\text{D}}(1) - 2\chi_{jk}^{\text{net}}(1)} \right) e^{-\chi_{kj}^{\text{net}}(1)} \left( 1 - e^{-\chi_{kj}^{\text{net}}(1)} \right) \right. \\
& \quad \left. + 2 \left( e^{-\hat{\chi}_{jjkk}^{\text{fan}}(1)} - e^{\tilde{\chi}_{jjkk}^{\text{D}(\text{l})}(1) - \chi_{jk}^{\text{net}}(1)} \right) e^{-2\chi_{kj}^{\text{net}}(1)} - 2 \left( \chi_{jk}^{\text{net}}(1) - \hat{\chi}_{jjkk}^{\text{fan}}(1) - \tilde{\chi}_{jjkk}^{\text{D}(\text{l})}(1) \right) \right] \\
& \quad \times \left[ \left( 1 - e^{2\tilde{\chi}_{kkjj}^{\text{D}}(2) - 2\chi_{kj}^{\text{net}}(2)} \right) e^{-\chi_{kj}^{\text{net}}(2)} \left( 1 - e^{-\chi_{kj}^{\text{net}}(2)} \right) + 2 \left( e^{-\hat{\chi}_{kkjj}^{\text{fan}}(2)} - e^{\tilde{\chi}_{kkjj}^{\text{D}(\text{l})}(2) - \chi_{kj}^{\text{net}}(2)} \right) \right. \\
& \quad \left. \left. \times e^{-2\chi_{kj}^{\text{net}}(2)} - 2 \left( \chi_{kj}^{\text{net}}(2) - \hat{\chi}_{kkjj}^{\text{fan}}(2) - \tilde{\chi}_{kkjj}^{\text{D}(\text{l})}(2) \right) \right] \right\}. \quad (56)
\end{aligned}$$

Here the arguments of the eikonals are understood as  $\chi_{jk}^{\text{net}}(i) = \chi_{jk}^{\text{net}}(Y - y_i, \vec{b} - \vec{b}_i | Y, \vec{b})$ ,  $\chi_{kj}^{\text{net}}(i) = \chi_{kj}^{\text{net}}(y_i, \vec{b}_i | Y, \vec{b})$ ,  $i = 1, 2$ , and similarly for  $\hat{\chi}^{\text{fan}}$ ,  $\tilde{\chi}^{\text{D}}$ ,  $\tilde{\chi}^{\text{D}(\text{l})}$ . Keeping only the lowest order contributions ( $\chi_{jk}^{\text{net}}, \hat{\chi}_{jjkk}^{\text{fan}} \rightarrow \chi_j^{\text{P}}$ ;  $\chi_{kj}^{\text{net}}, \hat{\chi}_{kkjj}^{\text{fan}} \rightarrow \chi_k^{\text{P}}$ ;  $\chi^{\text{loop}} \rightarrow \chi^{\text{P}}$ ;  $\tilde{\chi}^{\text{D}}, \tilde{\chi}^{\text{D}(\text{l})} \rightarrow 0$ ), Eq. (56) reduces to (29).

Let us now briefly discuss zigzag-like cut diagrams. While it has been shown in [12] that their contributions to the total cross section precisely cancel each other, it may not be obvious that they do not contribute to various diffractive topologies of final states. As an illustration, let us consider the two lowest order diagrams of that kind, which are depicted in Fig. 25 (a,b), whose

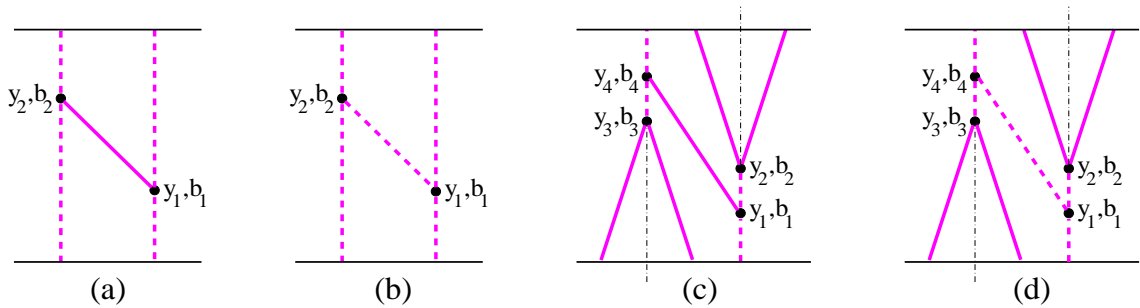


Figure 25: Examples of zigzag-like cut diagrams: lowest order ones (a,b) and the simplest graphs which give non-zero corrections to diffractive cross sections (c,d).

contributions are equal up to a sign. The diagram in Fig. 25 (a) provides a (negative) screening

correction to the eikonal configuration with two cut Pomerons. On the other hand, the one in Fig. 25 (b) introduces a new process, with the weight being equal to the one of the mentioned screening contribution, and with the particle production pattern being almost identical to the one of Fig. 25 (a); the only difference arises from the cut Pomeron exchanged between the vertices  $(y_1, b_1)$  and  $(y_2, b_2)$ . Thus, the combined effect of these two graphs is to provide additional particle production in the rapidity interval  $[y_1, y_2]$ . However, this interval is already covered by particles, which result from the left-most cut Pomeron in the two graphs. Thus, the rapidity gap structure of the event remains unchanged. The simplest diagrams which provide non-zero corrections to diffractive cross sections are the ones in Fig. 25 (c,d). The two contributions are again equal up to a sign, with the graph in Fig. 25 (c) providing a screening correction to double high mass diffraction cross section, with a LRG between  $y_2$  and  $y_3$ , and with the diagram in Fig. 25 (d) introducing additional particle production in the interval  $[y_1, y_4]$ , which covers the discussed rapidity gap. However, being proportional to the 4th power of the triple-Pomeron coupling, the corresponding contributions give a negligible correction to  $\sigma_{\text{HM}}^{\text{DD}}$ .

## References

- [1] V. N. Gribov, Sov. Phys. JETP **26**, 414 (1968); *ibid.* **29**, 483 (1969).
- [2] A. B. Kaidalov and K. A. Ter-Martirosyan, Phys. Lett. B **117**, 247 (1982); A. Capella *et al.*, Phys. Rep. **236**, 225 (1994).
- [3] P. Aurenche *et al.*, Phys. Rev. D **45**, 92 (1992); K. Werner, Phys. Rep. **232**, 87 (1993); N. N. Kalmykov and S. S. Ostapchenko, Phys. Atom. Nucl. **56**, 346 (1993); N. N. Kalmykov, S. S. Ostapchenko and A. I. Pavlov, Nucl. Phys. Proc. Suppl. **52B**, 17 (1997).
- [4] O. V. Kancheli, JETP Lett. **18**, 274 (1973); A. Schwimmer, Nucl. Phys. B **94**, 445 (1975); A. Capella, J. Kaplan and J. Tran Thanh Van, *ibid.* **105**, 333 (1976); V. A. Abramovskii, JETP Lett. **23**, 228 (1976); M. S. Dubovikov and K. A. Ter-Martirosyan, Nucl. Phys. B **124**, 163 (1977).
- [5] J. L. Cardi, Nucl. Phys. B **75**, 413 (1974).
- [6] A. B. Kaidalov, L. A. Ponomarev and K. A. Ter-Martirosyan, Sov. J. Nucl. Phys. **44**, 468 (1986).
- [7] V. A. Khoze, A. D. Martin and M. G. Ryskin, Eur. Phys. J. C **54**, 199 (2008); *ibid.* **60**, 249 (2009).
- [8] V. A. Khoze, A. D. Martin and M. G. Ryskin, Eur. Phys. J. C **60**, 265 (2009).
- [9] E. Gotsman, E. M. Levin, U. Maor and J. S. Miller, Eur. Phys. J. C **57**, 689 (2008); arXiv: 0901.1540.
- [10] S. Ostapchenko, Phys. Lett. B **636**, 40 (2006).
- [11] S. Ostapchenko, Phys. Rev. D **74**, 014026 (2006).
- [12] S. Ostapchenko, Phys. Rev. D **77**, 034009 (2008).
- [13] V. A. Abramovskii, V. N. Gribov and O. V. Kancheli, Sov. J. Nucl. Phys. **18**, 308 (1974).
- [14] A. B. Kaidalov, Phys. Rep. **50**, 157 (1979).
- [15] A. B. Kaidalov, V. A. Khoze, A. D. Martin and M. G. Ryskin, Eur. Phys. J. C **21**, 521 (2001).
- [16] M. Baker and K. A. Ter-Martirosian, Phys. Rep. **28**, 1 (1976).



- [17] V. A. Abramovskii and R. G. Betman, *Sov. J. Nucl. Phys.* **55**, 912 (1992).
- [18] CDF Collaboration, F. Abe *et al.*, *Phys. Rev. D* **50**, 5535 (1994).
- [19] E710 Collaboration, N. A. Amos *et al.*, *Phys. Rev. Lett.* **68**, 2433 (1992).
- [20] C. Caso *et al.*, *Eur. Phys. J.* **C3**, 1 (1998).
- [21] CDF Collaboration, F. Abe *et al.*, *Phys. Rev. D* **50**, 5550 (1994).
- [22] CDF Collaboration, T. Affolder *et al.*, *Phys. Rev. Lett.* **87**, 141802 (2001).
- [23] A. Breakstone *et al.*, *Nucl. Phys. B* **248**, 253 (1984).
- [24] UA1 Collaboration, R. Battiston *et al.*, *Phys. Lett.* **127B**, 472 (1983).
- [25] UA4 Collaboration, M. Bozzo *et al.*, *Phys. Lett.* **147B**, 385 (1985); *ibid.* **155B**, 197 (1985).
- [26] E710 Collaboration, N. A. Amos *et al.*, *Phys. Lett. B* **247**, 127 (1990).
- [27] CDF Collaboration, F. Abe *et al.*, *Phys. Rev. D* **50**, 5518 (1994).
- [28] D. Amati, A. Stanghellini and S. Fubini, *Nuovo Cim.* **26**, 896 (1962).
- [29] M. Braun, *Sov. J. Nucl. Phys.* **52**, 164 (1990); V. A. Abramovskii and G. G. Leptoukh, *ibid.* **55**, 903 (1992); M. Hladik, H. J. Drescher, S. Ostapchenko, T. Pierog and K. Werner, *Phys. Rev. Lett.* **86**, 3506 (2001).